

VARIFOLD MOMENT INVARIANTS FOR SUSTAINABLE AND EXPLAINABLE CONTOUR FEATURE EXTRACTION

G. LONGARI, J.-C. ÁLVAREZ PAIVA, AND A. B. TUMPACH

ABSTRACT. We introduce Varifold Moments Invariants (VMI) as a unifying framework for many previously introduced Moment Invariants. These invariants are deeply related to other contour features that are invariant under translations and rotations, like Extended Gaussian Image, Elliptic Fourier Descriptors or Shape Distributions. The advantage of the varifold approach to moments consists in being able to combine the geometry of the region, its boundary, and the family of lines tangent to it, in order to create a substantial number of invariant features with high discriminating power and clear geometric meaning. By coupling our VMI feature extraction with the light feature classifiers Random Forest or Multi-Layer-Perceptron, we outperform state-of-the-art approaches based on contours, while decreasing drastically the computational cost to the point of allowing our algorithm to run on light devices. We tested our approach on classification tasks on a large number of widely-used datasets of various types (leaves, objects, cells) and achieved high accuracy with a low number of geometrically interpretable features.

1. INTRODUCTION

Varifolds [1] are used in Computer Vision for shape registration and comparison [2, 3, 4, 5], surface reconstruction and discrete approximation of surfaces [6, 7], partial matching [8], atlas estimation of Functional Shapes [9], shape interpolation [10, 11], comparison and classification of shape sequences [12, 13], and have been generalized in [14].

In the present work, we introduce Varifold Moments and Shape Invariants related to them, called *Varifold Moment Invariants* (VMI). The present contribution leverages the theory of moments [15, 16, 17] to the varifold setting. We use this generalization to design high discriminating features of planar shapes bounded by simple closed curves modulo the action of a shape preserving group. Depending on the applications, this is the group of reparameterizations, translations, and rotations, which is sometimes extended by dilations. Two curves will represent the same shape if there exists a group element that transforms one curve into the other.

The invariants we introduce are products of *Varifold Moments*, i.e. integrals of the form

$$(1) \quad M(f; p, q, r) := \int_{\gamma} f(\kappa) z^p \bar{z}^q \left(\frac{\dot{z}}{|\dot{z}|} \right)^r |\dot{z}| dt,$$

where f is an arbitrary real-valued, piecewise-continuous function of the curvature κ , the powers $p, q \in \mathbb{N}$, $r \in \mathbb{Z}$, $z = x + iy$, and $|\dot{z}| dt$ the arc-length measure. These contour integrals allow us to define new geometric invariants as well as to provide a single framework for various classical moment invariants associated to different measures related to a curve (area measure of enclosed region, arc-length of the curve and extended Gaussian image). In particular our invariants encompass those in [15, 16, 17] and the Fourier coefficients of the extended Gaussian image [18, 19, 20, 21].

Many well-known Euclidean quantities associated to a curve γ can be expressed using these contour integrals. For example, the length, area, total curvature, curvature centroid, and moments (with respect to both the arc-length measure of the curve and the area measure of the enclosed region) can all be written as $M(f; p, q, r)$ for appropriate choices of f and integers p, q, r . Specifically, for a counter-clockwise oriented curve γ bounding a domain D , the length and area are given by

$$(2) \quad \text{Length}(\gamma) = M_{0,0,0} = \int_{\gamma} |\dot{z}| dt, \quad \text{Area}(\gamma) = \frac{1}{2i} M_{0,1,1} = \frac{1}{2i} \int_{\gamma} \bar{z} dt = \frac{1}{2i} \int_D d\bar{z} \wedge dz.$$

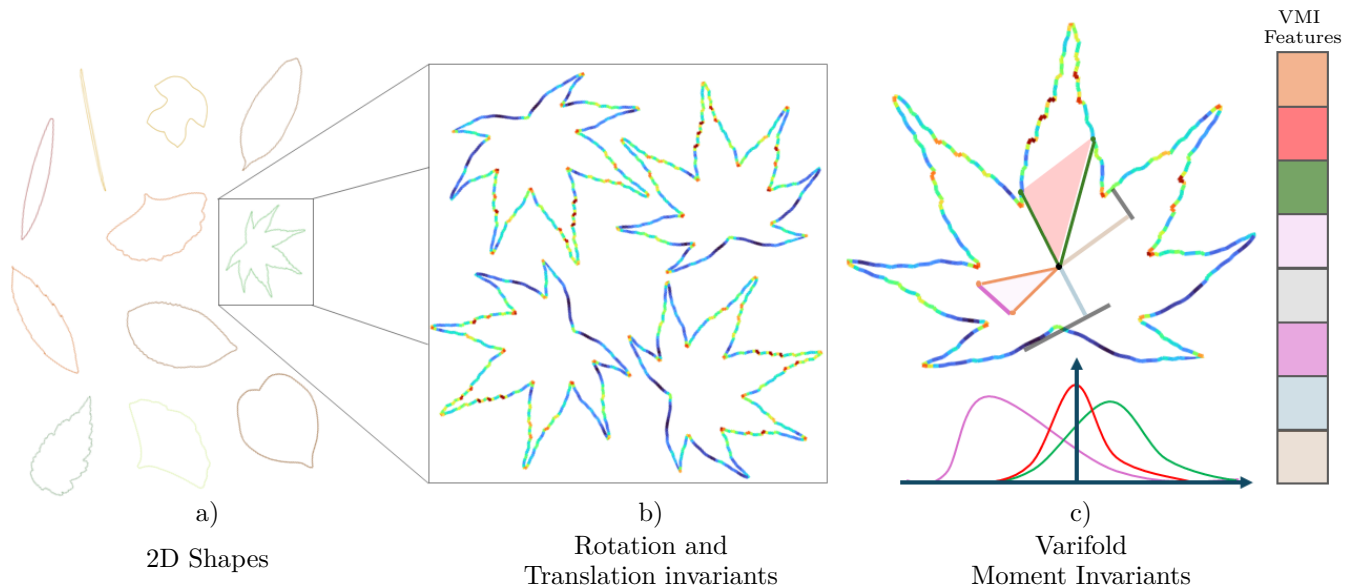


FIGURE 1. Given 2D contours of objects a), we seek features that are independent of their position and orientation on the plane b). The Varifold Moment Invariants are extracted from the polygonal representation of the curve and capture different geometric features of the shape such as the moments of various shape distributions (e.g., signed areas of random triangles or distances from random tangent and normal lines to the center of mass), yielding robust representations for machine learning tasks.

Complex moments (7) can also be expressed as this type of contour integrals [22]:

$$(3) \quad c_{p,q}(D) = \iint_D z^p \bar{z}^q dx dy = \frac{1}{2i(q+1)} \int_{\partial D} z^p \bar{z}^{q+1} dt = \frac{1}{2i(q+1)} M_{p,q+1,1}(\partial D).$$

We stress however that most varifold moments cannot be expressed in terms of their classical counterparts, even in the case where the curvature is not taken into account. For instance, the invariant moment $M(1;0,2,2)$ is not of this form. Geometrically, the classical moments associated to a region or curve consider points as their basic geometric objects, the extended Gaussian image considers unit tangent vectors deprived of their base points as the basic geometric objects, but in varifold moments the tangent unit vectors, base point and all, are considered. This allows us to associate Varifold Moment Invariants to the geometry of tangent and normal lines.

A key aspect of our approach that we found useful in feature design is that the moments of (1-dimensional) Shape distributions [23] such as mutual squared distances between random points, signed areas of random triangles or signed distances from tangent lines to the center of mass, can be expressed in terms of Varifold Moments. We found the mean, variance, skewness and kurtosis of these distributions to be discriminating Varifold Moment Invariants.

The main contributions of this paper are the following:

- we propose a unified theory of Moments, called Varifold Moments, that encompass Hu's Moments [15], Harmonic moments [24], Complex Moments [16, 17], Zernike Moments [25], on curves and planar domains;
- we use Varifold Moments to construct features that are invariant under translations, rotations and/or scaling, called Varifold Moment Invariants (VMI), that form a complete list of shape descriptors;
- we use geometric insight to design new discriminating invariant features, like the mean, variance, skewness and kurtosis of geometric distributions related to the shape of contours, expressed as Varifold Moment Invariants, allowing interpretability of feature selection.

- Due to high Discriminability and Robustness of invariants constructed as combinations of invariants for boundary measures, interior measures and Gaussian length measures, we propose algorithms with low environmental footprint.

2. RELATED WORK AND BASIC DEFINITIONS

2.1. Methods for invariance of Shape representations.

Extraction of invariant features. Features that are invariant or equivariant under translations and rotations can be extracted using Region Property features [26], Elliptic Fourier Descriptors [27, 19], Minkowski functionals [28, 29], Haralick features [30], Measures along Chord Bunches [31], Representation Theory of Groups [32, 33, 34], Invariant Moments [15, 17, 35, 36, 37, 38], Mutual Distances [39, 40], Gram-Matrices [41], Triangle Distance [42] [42], Multiscale Distance Matrices [43], integral invariant descriptors [44], multiscale curvature-based shape representation [45], or Shape distributions [23]. For domain specific classification, like leaves classification, multiple features extracted from shape, color and texture are usually combined [46]. Reviews of state-of-the-art methods for Leaf classification can be found in [47, 48], for cells in [49]. These methods can be coupled with machine learning algorithms like K -nearest-Neighbor [50, 38, 37, 42], Support Vector Machine [51, 35], ResNet-18 [52, 40], LeNet [53, 29], VGG16 [54, 55]. Since the features themselves remain invariant under the action of the shape-preserving group, the resulting algorithms achieve exact invariance.

Forcing invariance in Learning Algorithms. When the features extracted are not invariant under the action of the shape preserving group, invariance can be learned using data augmentation in the sample space [56], data augmentation in the feature space [57], prealignment [58] or modified convolutional neural networks [59, 60, 61, 62, 63, 64]. These methods usually suffer from high computational costs and are memory-intensive. Moreover, invariance is often only approximated, leading to the representation of shapes as multiple points in latent space (see Fig.2e in [58]).

2.2. Shape Moments, Moment Invariants and Shape Distributions.

Geometric Moments. Moments are the subject of many books [22, 65, 66] and review papers [67, 68]. Geometric moments of a density distribution function $\rho(x, y)$ in the plane are defined as the double sequence $m_{p,q}$ of Riemann integrals [69]

$$(4) \quad m_{p,q}(\rho) := \iint x^p y^q \rho(x, y) dx dy, \quad p, q = 0, 1, 2, \dots$$

By Weierstrass approximation theorem, the double sequence $\{m_{p,q}\}_{p,q \in \mathbb{N}}$ is **complete** in the sense that it completely characterizes piecewise continuous distribution functions $\rho(x, y)$ with bounded support, i.e. $\rho(x, y)$ is uniquely determined by its geometric moments. This is in particular the case for $\rho(x, y)$ equal to the indicatrix of a bounded domain in the plane, like the interior of a contour.

Central Moments. By setting $\bar{x} := m_{1,0}/m_{0,0}$ and $\bar{y} := m_{0,1}/m_{0,0}$, one can defined a double sequence of translation invariant moments, called **central moments**, as

$$(5) \quad \mu_{p,q}(\rho) := \iint (x - \bar{x})^p (y - \bar{y})^q \rho(x, y) dx dy, \quad p, q = 0, 1, 2, \dots$$

Orthogonal Moments. The geometric moments (4) can be thought as projections onto a sequence of monomials, which do not form an orthogonal basis for the L^2 -scalar product. In order to get a more efficient representation of shapes, orthogonal moments constructed as integrals over various sequences of orthogonal polynomials (for the L^2 -scalar product) were introduced. We refer the reader to Table 1 in the review paper [67] for a list of works introducing various orthogonal moments, including Legendre moments [70, 71], Zernike Moments [70] and Tchebichef Moments [72], and to Fig. 2 in [68] for a classification of various orthogonal moments used for image representations.

Harmonic Moments. Davis [24] studied the completeness of the sequence of moments defined as

$$(6) \quad \tau_n := \iint_D z^n dx dy,$$

where D is a bounded region in the complex plane, and shows that a triangle is uniquely determined by $\tau_1, \tau_2, \tau_3, \tau_4$. It was shown in [73] that harmonic moments of up to order $2n - 3$ allow to reconstruct a simply connected n -gon. For applications to tomography and geophysics see [73, 74].

Complex moments. Geometric moments are related to complex moments defined by [24]:

$$(7) \quad c_{p,q} := \iint_D z^p \bar{z}^q dx dy$$

More precisely, according to equation (1.4) and equation (1.5) in [24]

$$(8) \quad c_{p,q} = \sum_{j=0, k=0}^{p,q} (i)^{p-j} (i)^{q-k} \binom{p}{j} \binom{q}{k} m_{j+k, p+q-j-k},$$

$$(9) \quad m_{p,q} = (i)^n 2^{-p-q} \sum_{j=0, k=0}^{p,q} \binom{p}{j} \binom{q}{k} c_{j+k, p+q-j-k}.$$

It follows that a shape can be recovered from its complex moments. Some class of shapes can be recovered from a finite number of moments [75].

Moment Invariants for a group of transformations. A combination of moments will be called an (absolute) *Moment Invariant* for a group G , if it takes the same value on ρ and on all its transformations $g \cdot \rho$, $g \in G$, by the action of the group G . The central moments constitute an example of moments invariants for the group of translations.

The moment invariants constructed by Hu in [15] for the group of rotations are widely used in shape recognition tasks due to their simplicity and computational efficiency [76]. Hu also proposed a list of moment invariants for the affine group of transformations, which was corrected in [77]. Moment invariants for the other groups were proposed in [78, 79, 80]. In order to make use of the advantages of orthogonal basis of polynomials, some authors proposed to use Zernike moments to derive moments invariants [70, 81], and proved their completeness [25].

Abu-Mostafa and Psaltis [16] used complex moments (7) to define moment invariants for the translations and rotations, and analysed their discriminating power in practical situations.

In [82], the role of moments in image normalization and invariant pattern recognition was addressed.

Flusser [17] showed that the moments invariants proposed by Hu are functionally dependent and proposed a method to construct a basis of invariants for the rotation group, and proved its independence and completeness. Flusser and Suk [83] designed a complete and independent sequence of moment invariants for the affine group of transformations. In [84] a general method based on representation of invariants by graphs is proposed for automatic deriving affine moment invariants and eliminating reducible and dependent invariants.

Shape distributions. The idea to represent the signature of an object as a shape distribution is presented in [23] and exploited in [20] for convex sets. The characterization of a set of points by the distribution of all mutual distances has been addressed in [85]. Contrary to the case when the distances between pairs of points are known (exploited in Multidimensional Scaling technique for dimension reduction [86]), there exists non-reconstructible n -point configurations for any number of points and in any dimensions. However, for the vast majority of configurations, the position of points can be recovered from the distribution of mutual distances. The same holds for the distribution of areas of sub-triangles, which allows to reconstruct most configurations, though there are counterexamples.

3. PROPOSED APPROACH

3.1. Varifold Moments as unifying Framework.

Varifold Moments. Given a simple, closed, regular C^2 curve in the plane, $\gamma : [a, b] \rightarrow \mathbb{R}^2$, $t \mapsto \gamma(t)$, we introduce invariants defined as products of the following complex-valued contour integrals:

$$(10) \quad M(f; p, q, r) := \int_{\gamma} f(\kappa) z^p \bar{z}^q \left(\frac{\dot{z}}{|\dot{z}|} \right)^r |\dot{z}| dt,$$

where f is an arbitrary real-valued, piecewise-continuous function of the curvature κ , the powers $p, q \in \mathbb{N}$, $r \in \mathbb{Z}$, and $z = x + iy$. Because the integrand is homogenous of degree one in the velocities, these integrals, which we shall call *Varifold Moments*, are invariant under orientation-preserving reparametrizations of the curve, hence depends only on the shape of the curve and its orientation. Henceforth, we omit the function f when it is identically equal to 1 and write

$$(11) \quad M_{p,q,r}(\gamma) := \int_{\gamma} z^p \bar{z}^q \left(\frac{\dot{z}}{|\dot{z}|} \right)^r |\dot{z}| dt.$$

By equation (3), complex moments (7) can be recovered from the Varifold Moments (11). Consequently the sequence of Varifold Moments (11) is **complete**: it characterizes the contour uniquely, thereby making the Varifold Moments discriminating contour features.

Mathematical Interpretation of Varifold Moments. A (one-dimensional) *varifold* in \mathbb{R}^2 is a continuous linear functional on the space of continuous functions on $\mathbb{R}^2 \times \mathbb{S}^1$, which we identify with integrands that are homogeneous of degree one in the velocities.

Given a one-dimensional varifold V in \mathbb{R}^2 with compact support, we define the (p, q, r) -moment of V as

$$(12) \quad M_{p,q,r}(V) := \langle V | L_{p,q,r} \rangle,$$

where the integrand $L_{p,q,r}$ is defined by

$$(13) \quad L_{p,q,r} := z^p \bar{z}^q \left(\frac{\dot{z}}{|\dot{z}|} \right)^r |\dot{z}|.$$

Basic properties of varifold moments are listed in Appendix A.

Varifold Moment Invariants. A key advantage of the complex notation is its behaviour under rotation. If γ_{θ} denotes the rotated curve $t \mapsto e^{i\theta} \gamma(t)$, then

$$(14) \quad \int_{\gamma_{\theta}} f(\kappa) z^p \bar{z}^q \left(\frac{\dot{z}}{|\dot{z}|} \right)^r |\dot{z}| dt = e^{i(p-q+r)\theta} \int_{\gamma} f(\kappa) z^p \bar{z}^q \left(\frac{\dot{z}}{|\dot{z}|} \right)^r |\dot{z}| dt.$$

Consequently, any product

$$(15) \quad M(f_1; p_1, q_1, r_1) M(f_2; p_2, q_2, r_2) \cdots M(f_n; p_n, q_n, r_n)$$

satisfying

$$(16) \quad (p_1 - q_1 + r_1) + \cdots + (p_n - q_n + r_n) = 0$$

is invariant under rotations and defines a **rotation-invariant feature**. In order to obtain features that are also invariant by translation, we translate the curve so that the centre of mass of the enclosed domain lies at the origin. If we want to add invariance by scaling, we also normalize the area of the enclosed domain or the length of the curve (see [87] for the effect of different prealignment choices).

3.2. Geometric interpretation of discriminating Varifold Moments Invariants.

Moments of Shape Distributions as VMIs. Although the Varifold Moments Invariants form a complete list of invariants, we are seeking a low number of discriminating features that are invariant by translation and rotation. Some of these invariants are best described as moments of geometrically-defined statistical distributions. These one-dimensional distributions (random variables), which are themselves translation and rotation invariants of the curve, are particular in that their moments can be expressed as products of Varifold Moments. For instance, the first and second moments of the distribution of square distances between pairs of random points in the region D are given by

$$(17) \quad \frac{M_{1,2,1}(\partial D)}{M_{0,1,1}(\partial D)} \quad \text{and} \quad \frac{8M_{2,3,1}(\partial D)M_{0,1,1}(\partial D) + 2M_{1,2,1}(\partial D)^2 + 8M_{2,1,1}(\partial D)M_{0,3,1}(\partial D)}{12M_{0,1,1}(\partial D)^2},$$

respectively, assuming the center of mass of the region lies at the origin. As a second example, we consider the distribution of signed areas of triangles formed by random pairs of points on the curve and the center of mass. This distribution is symmetric about zero and its odd moments vanish. Its second and fourth moments are given by

$$\frac{M_{1,1,0}(\gamma)^2 - |M_{2,0,0}(\gamma)|^2}{2M_{0,0,0}(\gamma)^2} \quad \text{and} \quad \frac{|M_{4,0,0}(\gamma)|^2 - 4|M_{3,1,0}(\gamma)|^2 + 3M_{2,2,0}(\gamma)^2}{8M_{0,0,0}(\gamma)^2},$$

respectively. The reader will find details on the computations in Appendix B and on properties of Varifolds Moments in Appendix A. Searching for discriminating invariants with a clear geometric interpretation, we found a number of shape distributions whose moments are VMIs:

- *Square distance between two random points in the region.*
- *Square distance from a random point on the region to the center of mass.*
- *Square distance from a random point on curve to the center of mass.*
- *Signed distance from the center of mass to a random tangent line.*
- *Signed distance from a random point to a random tangent line.*
- *Signed distance from the center of mass to a random normal line.*
- *Distribution of signed areas of triangles formed by two random points in the region and the center of mass.*

The mean, variance, skewness, and kurtosis of these shape distributions are interesting geometric invariants and proved effective discriminators.

Classical geometric invariants as VMIs. Some invariants such as perimeter and area are useful when size matters, while other classical invariants such as the distance between the center of mass of the curve and the center of mass of the region it encloses ([88]) or the distance from the the cube of center of mass (considered as a complex number) to the centered third harmonic moment,

$$(18) \quad \left| \frac{\int_D (z - \text{center of mass})^3 dx dy}{\int_D dx dy} - \left(\frac{\int_D z dx dy}{\int_D dx dy} \right)^3 \right|,$$

are useful in detecting central symmetry. On the other hand, some new invariants such as the imaginary part of $M_{0,2,2}(\partial D)$ or the real part of $M_{0,3,3}(\partial D)$ are useful in detecting axial symmetry.

Curvature-weighted Varifold Moments. Finally, we made use of a number of VMIs that include the curvature function and its different discretizations [89, 90, 91]. They include the absolute total curvature, the Euler-Bernoulli functional (integral of the square curvature with respect to arc-length), and integrals of the form

$$(19) \quad HM_{p,q,r}(\gamma) := \int_{\gamma} \text{sgn}(\kappa) z^p \bar{z}^q \left(\frac{\dot{z}}{|\dot{z}|} \right)^r |\dot{z}| dt.$$

Here too, the varifold interpretation is key: a polygon can be interpreted as a varifold simply by being a collection of line segments over which to integrate, but an alternative interpretation is to integrate over the exterior angles. This viewpoint is already implicit in the definition of the total curvature of a polygon as the sum of its exterior angles and leads to the following varifold moments:

$$(20) \quad \bullet \sum_{j=0}^n |\mathbf{k}(z_{j-1}, z_j, z_{j+1})|^m, \text{ where}$$

$$\mathbf{k}(z_{j-1}, z_j, z_{j+1}) := \frac{2}{|z_{j+1} - z_j| + |z_j - z_{j-1}|} \left(\frac{z_{j+1} - z_j}{|z_{j+1} - z_j|} - \frac{z_j - z_{j-1}}{|z_j - z_{j-1}|} \right),$$

is a discretization of the mean curvature vector consisting of the difference of the two unit ‘‘tangent’’ vectors at the vertex z_j divided by the mean of the lengths of the edges $z_{j-1}z_j$ and z_jz_{j+1} ,

$$\bullet \sum_{j=0}^n z_j^p z_j^p (\theta_{j+1} - \theta_j)^m \quad (m \in \mathbb{N}),$$

$$\bullet \sum_{j=0}^n z_j^p z_j^{p+r} \left(\left(\frac{z_{j+1} - z_j}{|z_{j+1} - z_j|} \right)^r - \left(\frac{z_j - z_{j-1}}{|z_j - z_{j-1}|} \right)^r \right),$$

$$\bullet \sum_{j=0}^n \text{sgn}(\theta_{j+1} - \theta_j) z_j^p z_j^{p+r} \left(\left(\frac{z_{j+1} - z_j}{|z_{j+1} - z_j|} \right)^r - \left(\frac{z_j - z_{j-1}}{|z_j - z_{j-1}|} \right)^r \right).$$

Here the polygon γ is assumed to have vertices z_0, \dots, z_n , we have set $z_n = z_{-1}$, and defined the angles recursively by setting $\theta_0 \in [0, 2\pi)$ as the argument of $z_0 - z_{-1}$, and $\theta_{j+1} - \theta_j \in [0, 2\pi)$ for $0 \leq j \leq n$ as the argument of $(z_{j+1} - z_j)/(z_j - z_{j-1})$.

These new varifold moments also satisfy the equivariance property (14): when the curve is rotated by angle θ , the moment is multiplied by $e^{i(p-q+r)\theta}$.

4. EXPERIMENTS

4.1. Datasets. We performed our experiments using three types of shapes: *Geometric shapes and objects*, *Leaves* and *Cells*. We considered the following datasets (detailed in Appendix D):

- *Datasets of Geometric shapes and objects:*
 - **Mendeley:** 9 classes (triangles, circles and stars); 1000 samples per class.
 - **MNIST:** 10 classes (handwritten digits); 7000 samples per class.
 - **MPEG-7:** 70 classes (animals, tools); 20 samples per class.
 - **MPEG-400:** 20 classes (animals, household items); 20 samples per class.
- *Datasets of Leaves:*
 - **Swedish Leaves:** 15 classes, with 75 leaves per class.
 - **Flavia:** 1,907 leaf images belonging to 32 classes.
- *Dataset of Cells*
 - **BBBC010:** 2 classes with 768 individuals labeled alive, 639 labeled dead.
 - **HeLa Kyoto:** 313 cells divided in 4 classes.
 - **Mouse Osteosarcoma Cells (MOC):** 649 cells are divided in 3 classes.

4.2. Implementation details. Since our feature extractor is computationally lightweight (no GPU needed, see Appendix 4.2), we extracted both scale-invariant and scale-sensitive features, yielding 63 unique VMIs as robust shape descriptors. The code for extracting the VMI features and integrating them into a classification pipeline, along with the necessary tools for contour extraction and preprocessing (e.g., arc-length parametrization), is available at the following link: <TO ADD CODE LINK>. In all experiments, the classifier automatically identified the most informative features without any dataset specific prior knowledge. All the details on the classifiers used (Random Forest and Multi-layer Perceptron (MPL)) are provided in Appendix C.2.

4.3. Baselines and Evaluation. The proposed method is evaluated against state-of-the-art unsupervised invariant frameworks for 2D shape classification, including ShapeEmbed [40] based on ResNet-18 [92], and the recent Microsoft pipeline XShapeEncoder leveraging Zernike moments [36]. Additionally, we demonstrate improvements over the classical Flusser moment descriptor [83] and conventional computational baselines, namely Region Property features [26] and Elliptic Fourier Descriptors [19] (EFD). To evaluate the quality of the features extracted by our pipeline, we trained a Random Forest classifier [93] using a 5-fold stratified cross-validation strategy, with a 80/20 train-test split, reporting the mean and standard deviation of the F_1 -score [94, 95] across folds. The results are reported in Tables 1, 2 and 5.

TABLE 1. Classification results using F_1 -score (higher is better) on Objects datasets.

Method	MNIST [96]	MPEG-7 [97]	MPEG-400 [98]	Mendeley [99]
Flusser [83]	0.67 ± 0.00	0.54 ± 0.01	0.69 ± 0.03	0.68 ± 0.01
EFD [19]	0.89 ± 0.01	0.73 ± 0.03	0.86 ± 0.04	1 ± 0.00
Region Properties [26]	0.81 ± 0.00	0.89 ± 0.02	0.96 ± 0.02	0.99 ± 0.00
XShapeEncoder [36]	0.94 ± 0.00	0.87 ± 0.02	0.97 ± 0.02	1 ± 0.00
ShapeEmbed [40]	0.96 ± 0.01	0.75 ± 0.02	0.94 ± 0.04	1 ± 0.00
VMI + RF	0.90 ± 0.00	0.93 ± 0.02	0.98 ± 0.01	1 ± 0.00
VMI + MLP	0.95 ± 0.00	0.93 ± 0.01	0.99 ± 0.01	0.99 ± 0.00

TABLE 2. Classification results using F_1 -score (higher is better) on Leaves datasets.

Method	Flavia [100]	Swedish Leaves [101]
Flusser [83]	0.52 ± 0.02	0.52 ± 0.03
EFD [19]	0.75 ± 0.02	0.71 ± 0.03
Region Properties [26]	0.87 ± 0.01	0.84 ± 0.02
XShapeEncoder [36]	0.89 ± 0.02	0.86 ± 0.03
ShapeEmbed [40]	0.83 ± 0.03	0.79 ± 0.11
VMI + RF	0.96 ± 0.01	0.96 ± 0.01

4.4. Sustainability versus Performance. On most of the datasets, our algorithm outperforms the other methods, with a very low computational cost (see Table 3). Although ShapeEmbed give better classification rates on MNIST and BBBC010, it is computationally- and memory-intensive, and cannot be run on an ordinary laptop or embedded in a lighter devise. This limitation has at least two origins, the first one is the use of a modified ResNet-18 [92] where the standard convolutional and pooling operations have been replaced with layers that incorporate circular padding, the second is the use of distance matrices which scale as N^2 , where N is the number of points along contours. Consequently the number of points used to discretize contours is limited (set to 64 in the experiments presented in [40]) and an external server as to be booked to run the algorithm for many hours (48 hours for the MNIST dataset, whereas our algorithm runs for 3-4 hours on a computer, see Table 3). We argue that the gain in performance does not justify the use of such energy demanding algorithm.

TABLE 3. Comparison of average execution time for feature extraction versus average F_1 -score (higher is better) obtained for classification (the classification time is not counted; for VMI the classifier is MLP for MNIST, RF for MPEG-7 and Flavia).

Method	Hardware	MNIST [96] Duration/ F_1	MPEG-7 [97] Duration/ F_1	Flavia [100] Duration/ F_1
Flusser [83]	CPU	32 min /0.67	1 min /0.54	1 min /0.52
EFD [19]	CPU	3 min /0.89	5 sec /0.73	5 sec /0.75
Region Properties [26]	CPU	2 min /0.81	2 min /0.89	19 min /0.87
XShapeEncoder [36]	CPU	420 min /0.94	14 min/0.87	20 min/0.89
ShapeEmbed [40]	GPU	2,910 min / 0.96	270 min /0.75	270 min /0.83
VMI	CPU	210 min /0.95	5 min/ 0.93	8 min/ 0.96

4.5. Invariances Check. Since Varifold Moments are computed using cyclic sums over sample points of a curve, they are invariant under reindexing by design. They are also stable under the change of the number of points used for the discretization of the curve (Appendix G), as well as under addition of Gaussian noise (Appendix F).

To evaluate the invariance of VMI under rotations and translations, we construct augmented datasets by apply random rigid transformations to three datasets, MNIST, MPEG-7 and Flavia. Each contour

has been randomly rotated by an angle $\theta_i \sim \mathcal{U}(0^\circ, 360^\circ)$ around its centroid and followed by a random translation $(t_x^i, t_y^i) \sim \mathcal{U}(-50, 50)^2$. In Table 4 we refer to them as rMNIST, rMPEG-7 and rFlavia. From the results of Table 4 we can see that our pipeline, including prealigning the center of mass at the origin, is completely invariant under rotations and translations.

TABLE 4. Classification performance measured by F_1 -score (higher is better) on the rotated and translated datasets.

Method	rMNIST	rMPEG-7	rFlavia
XShapeEncoder [36]	0.76 ± 0.00	0.85 ± 0.02	0.85 ± 0.01
ShapeEmbed [40]	0.85 ± 0.01	0.66 ± 0.05	0.78 ± 0.05
VMI + RF	0.90 ± 0.00	0.93 ± 0.02	0.95 ± 0.01

4.6. Morphological Analysis of Biological Shapes. Contour analysis in biology often focuses on the study of cell shapes, a task that still requires substantial user input. Biologists typically inspect images individually, assisted by semi-automatic tools as well as manual procedures. While this approach is feasible for small datasets, it becomes impractical when dealing with millions of images, such as frames extracted from videos, where automation is essential. To address this challenge, methods such as [40] and [58] have been proposed, aiming to shift shape classification from manual analysis to automated pipelines. However, these approaches do not fully alleviate the significant time required for feature extraction and accurate classification across diverse cell types. In this section, we present experiments demonstrating that our method achieves strong classification performance while reducing computational cost and processing time (Table 3). We can observe in Table 5 that VMI succeed to extract meaningful features from contours also for small and not orientable dataset, without requiring information such as texture or color.

For the BBBC010 dataset, by exploiting a confident learning approach, we identified that approximately 7% of the samples are incorrectly or misleadingly labeled. Examples of these mislabeled instances are shown in the Appendix, Fig. 11. We therefore introduce a cleaned version of the dataset, denoted cBBBC010, which is used to evaluate the different approaches; the results are reported in Table 5. We observe that the F_1 -scores of all but one method improve on the cleaned dataset.

TABLE 5. Classification performance measured by F_1 -score (higher is better) on Cells datasets.

Method	BBBC010 [102]	cBBBC010 [102]	HeLa Kyoto [103]	MOC [104]
Flusser [83]	0.78 ± 0.02	0.85 ± 0.02	0.78 ± 0.05	0.67 ± 0.02
EFD [19]	0.81 ± 0.02	0.88 ± 0.02	0.55 ± 0.06	0.53 ± 0.03
Region Properties [26]	0.87 ± 0.03	0.93 ± 0.01	0.87 ± 0.04	0.70 ± 0.03
XShapeEncoder [36]	0.83 ± 0.02	0.92 ± 0.05	0.72 ± 0.04	0.52 ± 0.04
ShapeEmbed [40]	0.83 ± 0.00	0.84 ± 0.03	0.80 ± 0.04	0.68 ± 0.01
ShapeEmbed + Sz [40]	0.87 ± 0.01	0.82 ± 0.03	0.85 ± 0.04	0.70 ± 0.05
VMI + RF	0.85 ± 0.03	0.92 ± 0.02	0.91 ± 0.02	0.83 ± 0.02

5. CONCLUSION

In this work, we introduce Varifold Moments and use them to create high discriminative invariant features for shapes representations with a clear geometric meaning. We show that they provide compact and robust representation of shapes on classifications tasks that require invariance under reparameterization, translations, rotations, and/or scalings. We test our approach on various types of datasets (objects, leaves, cells). The resulting contour feature extraction algorithm coupled with light classifiers outperforms state-of-the-art algorithms with significantly lower computational costs. One limitation of our work is the handcrafted nature of the invariant features proposed. We envision that more discriminative Varifold Moment Invariants still have to be discovered. The extension of this framework to higher dimension is left for future work.

REFERENCES

- [1] William K. Allard. On the first variation of a varifold. *Annals of Mathematics*, 95:417–491, 1972.
- [2] Nicolas Charon and Alain Trouvé. The varifold representation of nonoriented shapes for diffeomorphic registration. *SIAM Journal on Imaging Sciences*, 6(4):2547–2580, 2013.
- [3] Irène Kaltenmark, Benjamin Charlier, and Nicolas Charon. A general framework for curve and surface comparison and registration with oriented varifolds. In *2017 IEEE Conference on Computer Vision and Pattern Recognition (CVPR)*, pages 4580–4589, 2017.
- [4] Nicolas Charon, Benjamin Charlier, Joan Glaunès, Pietro Gori, and Pierre Roussillon. 12 - fidelity metrics between curves and surfaces: currents, varifolds, and normal cycles. In Xavier Pennec, Stefan Sommer, and Tom Fletcher, editors, *Riemannian Geometric Statistics in Medical Image Analysis*, pages 441–477. Academic Press, 2020.
- [5] Kaitlin M. Stouffer, Xiaoyin Chen, Hongkui Zeng, Benjamin Charlier, Laurent Younes, Alain Trouvé, and Michael I. Miller. xiv-lddmm toolkit: A suite of image-varifold based technologies for representing and mapping 3d imaging and spatial-omics data simultaneously across scales. *bioRxiv*, 2024.
- [6] Blanche Buet, Gian Paolo Leonardi, and Simon Masnou. Discrete varifolds: A unified framework for discrete approximations of surfaces and mean curvature. In Jean-François Aujol, Mila Nikolova, and Nicolas Papadakis, editors, *Scale Space and Variational Methods in Computer Vision*, pages 513–524, Cham, 2015. Springer International Publishing.
- [7] Blanche Buet, Gian Paolo Leonardi, and Simon Masnou. A varifold approach to surface approximation. *Archive for Rational Mechanics and Analysis*, 226(2):639–694, 2017.
- [8] Pierre-Louis Antonsanti, Joan Glaunès, Thomas Benseghir, Vincent Jugnon, and Irène Kaltenmark. Partial matching in the space of varifolds. In Aasa Feragen, Stefan Sommer, Julia Schnabel, and Mads Nielsen, editors, *Information Processing in Medical Imaging*, pages 123–135, Cham, 2021. Springer International Publishing.
- [9] Benjamin Charlier, Nicolas Charon, and Alain Trouvé. The fshape framework for the variability analysis of functional shapes. *Foundations of Computational Mathematics*, 17(2):287–357, 2017.
- [10] Emmanuel Hartman, Emery Pierson, Martin Bauer, Mohamed Daoudi, and Nicolas Charon. Basis restricted elastic shape analysis on the space of unregistered surfaces. *International Journal of Computer Vision*, 133(4):1999–2024, 2025.
- [11] Martin Bauer, Martins Bruveris, Nicolas Charon, and Jacob Møller-Andersen. Varifold-based matching of curves via sobolev-type riemannian metrics. In *7th MICCAI workshop on Mathematical Foundations of Computational Anatomy*, 2017.
- [12] Emery Pierson, Mohamed Daoudi, and Sylvain Arguillere. 3d shape sequence of human comparison and classification using current and varifolds. In *Computer Vision ECCV 2022: 17th European Conference, Tel Aviv, Israel, October 23-27, 2022, Proceedings, Part III*, page 523539, Berlin, Heidelberg, 2022. Springer-Verlag.
- [13] Emery Pierson. *3D and 4D Human body surface comparison and deformation : from geometric invariants to Riemannian shape analysis*. PhD thesis, University of Lille, France, 2023.
- [14] Blanche Buet and Xavier Pennec. Flagfolds: an approach to multi-dimensional varifolds, 2023.
- [15] Ming-Kuei Hu. Visual pattern recognition by moment invariants. *IRE Transactions on Information Theory*, 8(2):179–187, 1962.
- [16] Yaser S. Abu-Mostafa and Demetri Psaltis. Recognitive aspects of moment invariants. *IEEE Transactions on Pattern Analysis and Machine Intelligence*, PAMI-6(6):698–706, 1984.
- [17] Jan Flusser. On the independence of rotation moment invariants. *Pattern Recognition*, 33(9):1405–1410, 2000.
- [18] Berthold K. P Horn. Extended gaussian images. *Proceedings of the IEEE*, 72(12):1671–1686, 1984.
- [19] Eric Persoon and King-Sun Fu. Shape discrimination using fourier descriptors. *IEEE Transactions on systems, man, and cybernetics*, 7(3):170–179, 2007.
- [20] Nicolas Charon and Thomas Pierron. On length measures of planar closed curves and the comparison of convex shapes. *Annals of Global Analysis and Geometry*, 60(4):863–901, 2021.
- [21] Emery Pierson, Juan-Carlos Álvarez Paiva, and Mohamed Daoudi. Projection-based classification of surfaces for 3d human mesh sequence retrieval. *Computers & Graphics*, 102:45–55, 2022.
- [22] Jan Flusser, Tomáš Suk, and Barbara Zitová. *Introduction to Moments*. John Wiley & Sons, Ltd, 2009.
- [23] Robert Osada, Thomas Funkhouser, Bernard Chazelle, and David Dobkin. Shape distributions. *ACM Trans. Graph.*, 21(4):807832, October 2002.
- [24] Philip J Davis. Plane regions determined by complex moments. *Journal of Approximation Theory*, 19(2):148–153, 1977.
- [25] Åke Wallin and Olaf Kübler. Complete sets of complex zernike moment invariants and the role of the pseudoinvariants. *IEEE Trans. Pattern Anal. Mach. Intell.*, 17(11):11061110, November 1995.
- [26] Stefan Van der Walt, Johannes L Schönberger, Juan Nunez-Iglesias, François Boulogne, Joshua D Warner, Neil Yager, Emmanuelle Gouillart, and Tony Yu. scikit-image: image processing in python. *PeerJ*, 2:e453, 2014.
- [27] Frank P Kuhl and Charles R Giardina. Elliptic fourier features of a closed contour. *Computer graphics and image processing*, 18(3):236–258, 1982.
- [28] Hermann Minkowski. Volumen und oberfläche. *Mathematische Annalen*, 57(4):447–495, 1903.
- [29] Natalie E P Lines, Joan Font-Quer Roset, and Anna M M Scaife. E(2)-equivariant features in machine learning for morphological classification of radio galaxies. *RAS Techniques and Instruments*, 3(1):347–361, 01 2024.
- [30] Robert M. Haralick, K. Shanmugam, and Its’Hak Dinstein. Textural features for image classification. *IEEE Transactions on Systems, Man, and Cybernetics*, SMC-3(6):610–621, 1973.

- [31] Bin Wang, Yongsheng Gao, Changming Sun, Michael Blumenstein, and John La Salle. Can walking and measuring along chord bunches better describe leaf shapes? In *2017 IEEE Conference on Computer Vision and Pattern Recognition (CVPR)*, pages 2047–2056, 2017.
- [32] Maurice Weiler and Gabriele Cesa. General $e(2)$ -equivariant steerable cnns. *Advances in Neural Information Processing Systems*, pages 14334–14345, 2019.
- [33] Sophia Sanborn and Nina Miolane. A general framework for robust g -invariance in g -equivariant networks. *Advances in Neural Information Processing Systems*, 36:67103–67124, 2023.
- [34] Simon Mataire, Johan Mathe, Sophia Sanborn, Christopher Hillar, and Nina Miolane. The selective g -bispectrum and its inversion: applications to g -invariant networks. In *Proceedings of the 38th International Conference on Neural Information Processing Systems, NIPS '24*, Red Hook, NY, USA, 2024. Curran Associates Inc.
- [35] Marko Lukic, Eva Tuba, and Milan Tuba. Leaf recognition algorithm using support vector machine with hu moments and local binary patterns. In *2017 IEEE 15th International Symposium on Applied Machine Intelligence and Informatics (SAMII)*, pages 000485–000490, 2017.
- [36] Yuhang He. Training-free spatially grounded geometric shape encoding (technical report). In *arXiv:2604.07522*, 2026.
- [37] Anant Bhardwaj, Manpreet Kaur, and Anupam Kumar. Recognition of plants by Leaf Image using Moment Invariant and Texture Analysis. *International Journal of Innovation and Applied Studies*, 3(1):237–248, 2013.
- [38] Zhuohao Jia and Simon Liao. Leaf recognition using k -nearest neighbors algorithm with zernike moments. In *2023 8th International Conference on Image, Vision and Computing (ICIVC)*, pages 665–669, 2023.
- [39] Anis Kacem, Mohamed Daoudi, Boulbaba Ben Amor, and Juan Carlos Alvarez-Paiva. A novel space-time representation on the positive semidefinite cone for facial expression recognition. In *2017 IEEE International Conference on Computer Vision (ICCV)*, pages 3199–3208, 2017.
- [40] Anna Foix Romero, Craig Russell, Alexander Krull, and Virginie Uhlmann. ShapeEmbed: a self-supervised learning framework for 2d contour quantification. In *The Thirty-ninth Annual Conference on Neural Information Processing Systems*, 2026.
- [41] Anis Kacem, Mohamed Daoudi, Boulbaba Ben Amor, Stefano Berretti, and Juan Carlos Alvarez-Paiva. A novel geometric framework on gram matrix trajectories for human behavior understanding. *IEEE Transactions on Pattern Analysis and Machine Intelligence*, 42(1):1–14, 2020.
- [42] Chengzhuan Yang and Hui Wei. Plant species recognition using triangle-distance representation. *IEEE Access*, 7:178108–178120, 2019.
- [43] Rongxiang Hu, Wei Jia, Haibin Ling, and Deshuang Huang. Multiscale distance matrix for fast plant leaf recognition. *IEEE Transactions on Image Processing*, 21(11):4667–4672, 2012.
- [44] Siddharth Manay, Daniel Cremers, Byung-Woo Hong, Anthony J Yezzi Jr, and Stefano Soatto. Integral invariants for shape matching. *IEEE Transactions on Pattern Analysis and Machine Intelligence*, 28(10):1602–1618, 2006.
- [45] Farzin Mokhtarian and Alan K Mackworth. A theory of multiscale, curvature-based shape representation for planar curves. *IEEE Transactions on Pattern Analysis and Machine Intelligence*, 14(8):789–805, 1992.
- [46] Boi M. Quach, V. Cuong Dinh, Nhung Pham, Dang Huynh, and Binh T. Nguyen. Leaf recognition using convolutional neural networks based features. *Multimedia Tools and Applications*, 82(1):777–801, 2023.
- [47] Zhaobin Wang, Jing Cui, and Ying Zhu. Review of plant leaf recognition. *Artificial Intelligence Review*, 56(5):4217–4253, 2023.
- [48] Christina Algemayel, Dany Abou Jaoude, Salma Talhouk, Ibrahim Issa, and Carine Ghassibe. Advances in machine learning models for plant species identification: A scoping review. *Ecological Informatics*, 93:103464, 2026.
- [49] Valentina Vadori, Antonella Peruffo, Jean-Marie Graïc, Livio Finos, and Enrico Grisan. Automated classification of cell shapes: A comparative evaluation of shape descriptors. *2025 IEEE 22nd International Symposium on Biomedical Imaging (ISBI)*, pages 1–4, 2024.
- [50] Evelyn Fix and Jr. JL Hodges. Discriminatory analysis. nonparametric discrimination: Consistency properties. *International Statistical Review / Revue Internationale de Statistique*, pages 238–247, 1989.
- [51] Corinna Cortes and Vladimir Vapnik. Support-vector networks. *Machine Learning*, 20(3):273–297, 1995.
- [52] Kaiming He, Xiangyu Zhang, Shaoqing Ren, and Jian Sun. Deep residual learning for image recognition. In *2016 IEEE Conference on Computer Vision and Pattern Recognition (CVPR)*, pages 770–778, 2016.
- [53] Yann LeCun, Leon Bottou, Yoshua Bengio, and Patrick Haffner. Gradient-based learning applied to document recognition. *Proceedings of the IEEE*, 86(11):2278–2324, 1998.
- [54] Karen Simonyan and Andrew Zisserman. Very deep convolutional networks for large-scale image recognition. *CoRR*, abs/1409.1556, 2014.
- [55] Ervin Gubin Moug, Chong Joon Hou, Maisarah Mohd Sufian, Mohd Hanafi Ahmad Hijazi, Jamal Ahmad Dargham, and Sigeru Omatu. Fusion of moment invariant method and deep learning algorithm for covid-19 classification. *Big Data and Cognitive Computing*, 5(4), 2021.
- [56] Sander Dieleman, Kyle W. Willett, and Joni Dambre. Rotation-invariant convolutional neural networks for galaxy morphology prediction. *Monthly Notices of the Royal Astronomical Society*, 450(2):1441–1459, 06 2015.
- [57] Dinesh Kumar, Dharmendra Sharma, and Roland Goecke. Feature map augmentation to improve rotation invariance in convolutional neural networks. In Jacques Blanc-Talon, Patrice Delmas, Wilfried Philips, Dan Popescu, and Paul Scheunders, editors, *Advanced Concepts for Intelligent Vision Systems*, pages 348–359, Cham, 2020. Springer International Publishing.

- [58] James Burgess, Jeffrey J. Nirschl, Maria-Clara Zanellati, Alejandro Lozano, Sarah Cohen, and Serena Yeung-Levy. Orientation-invariant autoencoders learn robust representations for shape profiling of cells and organelles. *Nature Communications*, 15(1):1022, 2024.
- [59] Taco Cohen and Max Welling. Group equivariant convolutional networks. In Maria Florina Balcan and Kilian Q. Weinberger, editors, *Proceedings of The 33rd International Conference on Machine Learning*, volume 48 of *Proceedings of Machine Learning Research*, pages 2990–2999, New York, New York, USA, 20–22 Jun 2016. PMLR.
- [60] Marc Finzi, Samuel Stanton, Pavel Izmailov, and Andrew Gordon Wilson. Generalizing convolutional neural networks for equivariance to lie groups on arbitrary continuous data. In Hal Daumé III and Aarti Singh, editors, *Proceedings of the 37th International Conference on Machine Learning*, volume 119 of *Proceedings of Machine Learning Research*, pages 3165–3176. PMLR, 13–18 Jul 2020.
- [61] Maurice Weiler, Fred A. Hamprecht, and Martin Storath. Learning steerable filters for rotation equivariant cnns. In *2018 IEEE/CVF Conference on Computer Vision and Pattern Recognition*, pages 849–858, 2018.
- [62] Bart M. N. Smets, Jim Portegies, Erik J. Bekkers, and Remco Duits. Pde-based group equivariant convolutional neural networks. *Journal of Mathematical Imaging and Vision*, 65(1):209–239, 2023.
- [63] Erik J. Bekkers, Maxime W. Lafarge, Mitko Veta, Koen A. J. Eppenhof, Josien P. W. Pluim, and Remco Duits. Roto-translation covariant convolutional networks for medical image analysis. In *Medical Image Computing and Computer Assisted Intervention MICCAI 2018: 21st International Conference, Granada, Spain, September 16-20, 2018, Proceedings, Part I*, page 440448, Berlin, Heidelberg, 2018. Springer-Verlag.
- [64] Odin Hoff Gardaa and Nello Blaser. Rotatouille: Rotation equivariant deep learning for contours, 2025.
- [65] Jan Flusser, Tomáš Suk, and Barbara Zitová. *2D and 3D Image Analysis by Moments*. John Wiley & Sons, Ltd, 2016.
- [66] Joseph L. Mundy and Andrew Zisserman. *Geometric Invariance in Computer Vision, Artificial Intelligence*. MIT Press, Cambridge, MA, 1992.
- [67] Mohd Wafi Nasrudin, Nizam Shahrul Yaakob, Nazren Amir Abdul Rahim, Mohd Zamri Zahir Ahmad, Nuraminah Ramli, and Mohd Shaiful Aziz Rashid. Moment invariants technique for image analysis and its applications: A review. *Journal of Physics: Conference Series*, 1962(1):012028, jul 2021.
- [68] Shuren Qi, Yushu Zhang, Chao Wang, Jiantao Zhou, and Xiaochun Cao. A survey of orthogonal moments for image representation: Theory, implementation, and evaluation. *ACM Comput. Surv.*, 55(1), November 2021.
- [69] Edward John Routh. *An elementary treatise on the dynamics of a system of rigid bodies*. London ; New York : Macmillan, 1905.
- [70] Michael Reed Teague. Image analysis via the general theory of moments. *Journal of the Optical Society of America (1917-1983)*, 70(8):920, August 1980.
- [71] Simon X. Liao and Miroslaw Pawlak. On image analysis by moments. *IEEE Trans. Pattern Anal. Mach. Intell.*, 18(3):254266, March 1996.
- [72] Ramakrishnan Mukundan, Seng-Huat Ong, and P.A. Lee. Image analysis by tchebichef moments. *IEEE Transactions on Image Processing*, 10(9):1357–1364, 2001.
- [73] Peyman Milanfar, George C. Verghese, William Clem Karl, and Alan S. Willsky. Reconstructing polygons from moments with connections to array processing. *Trans. Sig. Proc.*, 43(2):432443, February 1995.
- [74] Gene H. Golub, Peyman Milanfar, and James Varah. A stable numerical method for inverting shape from moments. *SIAM Journal on Scientific Computing*, 21(4):1222–1243, 1999.
- [75] Björn Gustafsson, Chiyu He, Peyman Milanfar, and Mihai Putinar. Reconstructing planar domains from their moments. *Inverse Problems*, 16(4):1053, aug 2000.
- [76] David R. Stirling, Madison J. Swain-Bowden, Alice M. Lucas, Anne E. Carpenter, Beth A. Cimini, and Allen Goodman. Cellprofiler 4: improvements in speed, utility and usability. *BMC Bioinformatics*, 22(1):433, 2021.
- [77] Thomas H. Reiss. The revised fundamental theorem of moment invariants. *IEEE Transactions on Pattern Analysis and Machine Intelligence*, 13(8):830–834, 1991.
- [78] Mark S. Hickman. Geometric moments and their invariants. *Journal of Mathematical Imaging and Vision*, 44(3):223–235, 2012.
- [79] Tomáš Suk and Jan Flusser. Projective moment invariants. *IEEE Transactions on Pattern Analysis and Machine Intelligence*, 26(10):1364–1367, 2004.
- [80] Wang Yuanbin, Zhang Bin, and Yao Tianshun. Projective invariants of co-moments of 2d images. *Pattern Recognition*, 43(10):3233–3242, 2010.
- [81] Saad O. Belkasim, Malayappan Shridhar, and Majid Ahmadi. Pattern recognition with moment invariants: A comparative study and new results. *Pattern Recognition*, 24(12):1117–1138, 1991.
- [82] Yaser S. Abu-Mostafa and Demetri Psaltis. Image normalization by complex moments. *IEEE Transactions on Pattern Analysis and Machine Intelligence*, PAMI-7:46–55, 1985.
- [83] Jan Flusser and Tomáš Suk. Pattern recognition by affine moment invariants. *Pattern Recognition*, 26(1):167–174, 1993.
- [84] Tomáš Suk and Jan Flusser. Affine moment invariants generated by graph method. *Pattern Recognition*, 44(9):2047–2056, 2011. *Computer Analysis of Images and Patterns*.
- [85] Mireille Boutin and Gregor Kemper. On reconstructing n-point configurations from the distribution of distances or areas. *Advances in Applied Mathematics*, 32(4):709–735, 2004.
- [86] Joseph B. Kruskal. Multidimensional scaling by optimizing goodness of fit to a nonmetric hypothesis. *Psychometrika*, 29(1):1–27, 1964.

- [87] Ioana Ciuclea, Giorgio Longari, and Alice Barbora Tumpach. Geometric learning of canonical parameterizations of 2d-curves. *Entropy*, 28(1), 2026.
- [88] Fedor Nazarov, Dmitry Ryabogin, and Vladyslav Yaskin. On the maximal distance between the centers of mass of a planar convex body and its boundary. *Discrete Comput Geom*, 73:1016–1036, 2025.
- [89] Keenan Crane and Max Wardetzky. A glimpse into discrete differential geometry. *Notices of the American Mathematical Society*, 64(10), 2017.
- [90] Ivan Izmestiev. Discrete curvature, 2025.
- [91] Sebastian Scholtes, Henrik Schumacher, and Max Wardetzky. Variational convergence of discrete elasticae. *IMA Journal of Numerical Analysis*, 2019.
- [92] Kaiming He, Xiangyu Zhang, Shaoqing Ren, and Jian Sun. Deep residual learning for image recognition. In *Proceedings of the IEEE conference on computer vision and pattern recognition*, pages 770–778, 2016.
- [93] Leo Breiman. Random forests. *Machine Learning*, 45(1):5–32, 2001.
- [94] David C. Blair. Information retrieval, 2nd ed. c.j. van rijnsbergen. london: Butterworths; 1979: 208 pp. price: \$32.50. *Journal of the American Society for Information Science*, 30(6):374–375, 1979.
- [95] Peter Christen, David J. Hand, and Nishadi Kirielle. A review of the f-measure: Its history, properties, criticism, and alternatives. *ACM Comput. Surv.*, 56(3), October 2023.
- [96] Li Deng. The mnist database of handwritten digit images for machine learning research [best of the web]. *IEEE signal processing magazine*, 29(6):141–142, 2012.
- [97] Richard Ralph. Mpeg-7 core experiment ce-shape-1. Technical report, ISO/IEC JTC1/SC29/WG11, 1999.
- [98] Longin Jan Latecki and Rolf Lakamper. Shape similarity measure based on correspondence of visual parts. *IEEE Transactions on Pattern Analysis and Machine Intelligence*, 22(10):1185–1190, 2002. MPEG-400 shape dataset.
- [99] Anas El Korchi and Youssef Ghanou. 2d geometric shapes dataset for machine learning and pattern recognition. *Data in Brief*, 32:106090, 2020.
- [100] Stephen Gang Wu, Forrest Sheng Bao, Eric You Xu, Yu-Xuan Wang, Yi-Fan Chang, and Qiao-Liang Xiang. A leaf recognition algorithm for plant classification using probabilistic neural network. In *2007 IEEE international symposium on signal processing and information technology*, pages 11–16. IEEE, 2007. FLAVIA dataset. Accessed: 2026-04-20.
- [101] Oskar J. O. Söderkvist. Computer vision classification of leaves from swedish trees. Master’s thesis, Linköping University, 2001. Swedish Leaf Dataset. Accessed: 2026-03-04.
- [102] Vebjorn Ljosa, Katherine L Sokolnicki, and Anne E Carpenter. Annotated high-throughput microscopy image sets for validation. *Nature methods*, 9(7):637, 2012. Broad Bioimage Benchmark Collection (BBBC010).
- [103] Michael Held, Michael HA Schmitz, Bernd Fischer, Thomas Walter, Beate Neumann, Michael H Olma, Matthias Peter, Jan Ellenberg, and Daniel W Gerlich. Cellcognition: time-resolved phenotype annotation in high-throughput live cell imaging. *Nature methods*, 7(9):747–754, 2010. HeLa Kyoto dataset.
- [104] Nina Miolane, Nicolas Guigui, Alice Le Brigant, Johan Mathe, Benjamin Hou, Yann Thanwerdas, Stefan Heyder, Olivier Peltre, Niklas Koep, Hadi Zaatiti, et al. Geomstats: A python package for riemannian geometry in machine learning. *Journal of Machine Learning Research*, 21(223):1–9, 2020. Mouse Osteosarcoma Cells (MOC) dataset.
- [105] Luis A Santaló. *Integral geometry and geometric probability*. Cambridge university press, 2004.
- [106] Isabelle Guyon, Jason Weston, Stephen Barnhill, and Vladimir Vapnik. Gene selection for cancer classification using support vector machines. *Machine learning*, 46(1):389–422, 2002.
- [107] Adam Paszke, Sam Gross, Francisco Massa, Adam Lerer, James Bradbury, Gregory Chanan, Trevor Killeen, Zeming Lin, Natalia Gimelshein, Luca Antiga, et al. Pytorch: An imperative style, high-performance deep learning library. *Advances in neural information processing systems*, 32, 2019.
- [108] Sergey Ioffe and Christian Szegedy. Batch normalization: Accelerating deep network training by reducing internal covariate shift. In *International conference on machine learning*, pages 448–456. pmlr, 2015.
- [109] Vinod Nair and Geoffrey E Hinton. Rectified linear units improve restricted boltzmann machines. In *Proceedings of the 27th international conference on machine learning (ICML-10)*, pages 807–814, 2010.
- [110] Nitish Srivastava, Geoffrey Hinton, Alex Krizhevsky, Ilya Sutskever, and Ruslan Salakhutdinov. Dropout: a simple way to prevent neural networks from overfitting. *The journal of machine learning research*, 15(1):1929–1958, 2014.
- [111] Ekaba Bisong. Logistic regression. In *Building machine learning and deep learning models on google cloud platform: A comprehensive guide for beginners*, pages 243–250. Springer, 2019.

APPENDIX A. PROPERTIES OF VARIFOLD MOMENTS

If γ is a C^1 regular curve, the moments $M_{p,q,r}(\gamma)$ satisfy the following basic properties.

Property 1. $M_{p,q,r}(\gamma)$ is independent of the parametrization of γ .

Property 2. If γ is the concatenation of curves $\gamma_0, \dots, \gamma_n$, then

$$M_{p,q,r}(\gamma) = \sum_{j=0}^n M_{p,q,r}(\gamma_j).$$

Property 3. The conjugate of $M_{p,q,r}(\gamma)$ is given by $M_{q,p,-r}(\gamma)$.

Property 4. If γ is a closed curve, then

$$M_{p,0,1}(\gamma) = \int_{\gamma} z^p \left(\frac{\dot{z}}{|\dot{z}|} \right) |\dot{z}| dt = \int_{\gamma} z^p dz = 0$$

for every $p \in \mathbb{N}$, since it is the integral of a holomorphic function over a closed path.

Property 5. If γ is a closed curve and p and q are natural numbers with $q > 0$, then

$$\overline{M_{p,q,1}(\gamma)} = -\frac{q}{p+1} M_{q-1,p+1,1}(\gamma).$$

An immediate consequence of this property is that *whenever γ is a closed curve, the varifold moment $M_{p,p+1,1}(\gamma)$ is purely imaginary.*

Property 6. If γ_{θ} denotes the curve γ rotated counter-clockwise by an angle θ , then

$$M_{p,q,r}(\gamma_{\theta}) = e^{i(p-q+r)\theta} M_{p,q,r}(\gamma).$$

This follows immediately from the identity $\gamma_{\theta}(t) = e^{i\theta}\gamma(t)$, but has some important consequences:

- If for some $\theta \not\equiv 0 \pmod{2\pi}$, $\gamma_{\theta} = \gamma$ (i.e., the curve γ has a non-trivial rotational symmetry) and $(p-q+r)\theta$ is not a multiple of 2π , then $M_{p,q,r}(\gamma) = 0$. In particular, if the curve γ is centrally symmetric and $p-q+r$ is odd, then $M_{p,q,r}(\gamma) = 0$.
- If $p-q+r = 0$, then the moment $M_{p,q,r}(\gamma)$ is invariant under rotations of γ .
- More generally, if for $1 \leq j \leq n$ the numbers p_j and q_j are natural numbers and the numbers r_j are integers such that

$$(p_1 - q_1 + r_1) + (p_2 - q_2 + r_2) + \dots + (p_n - q_n + r_n) = 0,$$

then the product $M_{p_1,q_1,r_1}(\gamma)M_{p_2,q_2,r_2}(\gamma) \cdots M_{p_n,q_n,r_n}(\gamma)$ is a rotation invariant of γ .

Property 7. If $\bar{\gamma}$ denotes the image of the parametrized curve γ under conjugation, then

$$M_{p,q,r}(\bar{\gamma}) = \overline{M_{p,q,r}(\gamma)}.$$

In particular, if *as a point set* the curve γ is invariant under reflection across the x -axis, then the varifold moment $M_{p,q,r}(\gamma)$ will be real when r is even and purely imaginary when r is odd.

APPENDIX B. GEOMETRIC PROBABILITIES AND VARIFOLD MOMENTS

Given a region of finite area D in the Euclidean plane, the statistical distribution of mutual distances between pairs of points in D defines a probability measure on the real line that is itself a Euclidean invariant of D . Another example of an invariant probability measure associated with D is the statistical distribution of the areas of all triangles with vertices in D . The study of these distributions is part of classical integral geometry (see, for instance, [105]) and their use in the classification of shapes was pioneered in [23].

In this section we present a number of invariant statistical distributions associated with piecewise C^1 curves on the plane and show that their moments—which are numerical Euclidean invariants of the curve—can be computed in terms of varifold moments.

Distributions of mutual square distances. If we wish to use the distribution of square distances between pairs of points to construct Euclidean invariants, we have the choice of taking the points in the region D or restricting to pairs of points on its boundary. For both choices, their moments are easily expressed in terms of varifold moments.

Up to division by the square of the area of D , the n -th moment for the statistical distribution of square distances between pairs of points in D is given by

$$\begin{aligned} & \frac{-1}{4} \iint_{D \times D} |z - w|^{2n} d\bar{z} \wedge dz \wedge d\bar{w} \wedge dw = \\ & \frac{-1}{4} \iint_{D \times D} (z\bar{z} - z\bar{w} - w\bar{z} + w\bar{w})^n d\bar{z} \wedge dz \wedge d\bar{w} \wedge dw, \end{aligned}$$

which results in a sum of separable integrands and a sum of varifold moment invariants. For example, momentarily forgetting the factor $-1/4$, the mean of the mutual square distances is given by

$$\begin{aligned} & \iint_{D \times D} (z\bar{z} - z\bar{w} - w\bar{z} + w\bar{w}) d\bar{z} \wedge dz \wedge d\bar{w} \wedge dw \\ &= \int_D z\bar{z} d\bar{z} \wedge dz \int_D d\bar{w} \wedge dw - \int_D z d\bar{z} \wedge dz \int_D \bar{w} d\bar{w} \wedge dw \\ & - \int_D \bar{z} d\bar{z} \wedge dz \int_D w d\bar{w} \wedge dw + \int_D w\bar{w} d\bar{w} \wedge dw \int_D d\bar{z} \wedge dz \\ &= M_{1,2,1}(\gamma) M_{0,1,1}(\gamma) - M_{1,1,1}(\gamma) M_{0,2,1}(\gamma). \end{aligned}$$

Reintroducing the factor $-1/4$ and dividing by the square of the area of D , we have that *the mean square distance between pairs of points in D is given by the expression*

$$\frac{M_{1,2,1}(\gamma) M_{0,1,1}(\gamma) - M_{1,1,1}(\gamma) M_{0,2,1}(\gamma)}{M_{0,1,1}(\gamma)^2}.$$

However, if the center of mass of the region lies at the origin, then $M_{1,1,1}(\gamma) = 0$ and the expression simplifies to

$$\frac{M_{1,2,1}(\gamma)}{M_{0,1,1}(\gamma)}.$$

Also assuming the center of mass is at the origin, the second moment of this distribution is given by

$$\frac{8M_{2,3,1}(\gamma)M_{0,1,1}(\gamma) + 2M_{1,2,1}(\gamma)^2 + 8M_{2,1,1}(\gamma)M_{0,3,1}(\gamma)}{12M_{0,1,1}(\gamma)^2}.$$

Other interesting quantities associated with the distribution of mutual square distances are its variance, skewness, and kurtosis, computed in terms of its second, third, and fourth central moments. These can all be computed in terms of varifold moments.

Up to division by the square of the perimeter of γ , the n -th moment for the statistical distribution of square distances between pairs of points of the curve γ is given by

$$\iint_{\gamma \times \gamma} |z(s_1) - w(s_2)|^{2n} ds_1 ds_2.$$

In the same way as before, this integral is a sum of separable integrands and can be written as a sum of varifold moment invariants.

$$\begin{aligned}
& \iint_{\gamma \times \gamma} |z(s_1) - z(s_2)|^2 ds_1 ds_2 \\
&= \iint_{\gamma \times \gamma} (z(s_1)\bar{z}(s_1) - z(s_1)\bar{z}(s_2) - z(s_2)\bar{z}(s_1) + z(s_2)\bar{z}(s_2)) ds_1 ds_2 \\
&= \int_{\gamma} z(s_1)\bar{z}(s_1) ds_1 \int_{\gamma} ds_2 - \int_{\gamma} z(s_1) ds_1 \int_{\gamma} \bar{z}(s_2) ds_2 \\
&\quad - \int_{\gamma} \bar{z}(s_1) ds_1 \int_{\gamma} z(s_2) ds_2 + \int_{\gamma} ds_1 \int_{\gamma} z(s_2)\bar{z}(s_2) ds_2 \\
&= 2(M_{1,1,0}(\gamma)M_{0,0,0}(\gamma) - M_{1,0,0}(\gamma)M_{0,1,0}(\gamma)).
\end{aligned}$$

We conclude that the mean square distance between pairs of points on γ is given by

$$\frac{2(M_{1,1,0}(\gamma)M_{0,0,0}(\gamma) - M_{1,0,0}(\gamma)M_{0,1,0}(\gamma))}{M_{0,0,0}(\gamma)^2}.$$

The mean, variance, skewness, and kurtosis of the distribution of square distances for pairs of points on γ proved very useful in our experiments.

Notice that *the n -th moment of the distribution of square distances from a random point of D to the origin is given by*

$$\frac{\iint_D |z|^{2n} dx dy}{\iint_D dx dy} = \frac{M_{n,n+1,1}(\gamma)}{(n+1)M_{0,1,1}(\gamma)}.$$

In our experiments we have translated all curves so that their center of mass lies at the origin, so these numbers are also Euclidean invariants.

Similarly, *the n -th moment of the distribution of square distances from a random point on γ to the origin is given by*

$$\frac{\int_{\gamma} |z|^{2n} ds}{\int_{\gamma} ds} = \frac{M_{n,n,0}(\gamma)}{M_{0,0,0}(\gamma)}.$$

Centered moments, which are also Euclidean invariants, are obtained from these moments by the standard formulas.

Distribution of signed areas of triangles. Just as with mutual distances, there are various statistical distributions we can associate with areas of triangles with vertices on a region or on its boundary.

Given three points z_0 , z_1 , and z_2 in D , the signed area of the triangle $\Delta z_0 z_1 z_2$ is given as one-half the determinant of the vectors $(z_1 - z_0)$ and $(z_2 - z_0)$, which can also be expressed as $\Im((\bar{z}_1 - \bar{z}_0)(z_2 - z_0))$.

The n -th moment of the distribution of signed areas of triangles with vertices in D equals the integral

$$\frac{-1}{8i} \iiint_{D \times D \times D} \Im((\bar{z}_1 - \bar{z}_0)(z_2 - z_0))^n d\bar{z}_1 \wedge dz_1 \wedge d\bar{z}_2 \wedge dz_2 \wedge d\bar{z}_0 \wedge dz_0$$

divided by the product of 2^n and the cube of the area of D . Just as in the case of mutual square distances, this integral breaks down into a sum of integrals of separable integrands, which can be easily expressed in terms of complex or varifold moments. Since interchanging z_1 and z_2 changes the sign of the area, this distribution is symmetric about 0, and only even moments yield interesting invariants. Moreover, these moments are not only invariant under the Euclidean group, but also invariant under the group of unimodular affine transformations.

A simpler distribution of signed areas is that of triangles formed by two random points on D and its center of mass, which we assume to be the origin. This distribution is also symmetric about zero, but its variance and kurtosis proved useful in our experiments.

Up to a factor of $-1/16$ and division by the square of the area of D , the variance is given by the integral

$$\begin{aligned}
 & \iint_{D \times D} \Im(\bar{z}w)^2 d\bar{z} \wedge dz \wedge d\bar{w} \wedge dw \\
 &= \frac{-1}{4} \iint_{D \times D} (\bar{z}w - z\bar{w})^2 d\bar{z} \wedge dz \wedge d\bar{w} \wedge dw \\
 &= \frac{-1}{4} \iint_{D \times D} (\bar{z}^2 w^2 - 2|z|^2 |w|^2 + z^2 \bar{w}^2) d\bar{z} \wedge dz \wedge d\bar{w} \wedge dw \\
 &= \frac{-1}{2} \int_D \bar{z}^2 d\bar{z} \wedge dz \int_D w^2 d\bar{w} \wedge dw + \frac{1}{2} \left(\int_D |z|^2 d\bar{z} \wedge dz \right)^2 \\
 &= \frac{-1}{6} M_{0,3,1}(\gamma) M_{2,1,1}(\gamma) + \frac{1}{8} M_{1,2,1}(\gamma)^2.
 \end{aligned}$$

The variance of the distribution of signed areas of triangles formed by pairs of random points in D and the center of mass is given by

$$\frac{-M_{0,3,1}(\gamma) M_{2,1,1}(\gamma)/6 + M_{1,2,1}(\gamma)^2/8}{8M_{0,1,1}(\gamma)^2} = \frac{-|M_{0,3,1}(\gamma)|^2/9 + M_{1,2,1}(\gamma)^2/4}{16M_{0,1,1}(\gamma)^2},$$

where we used the identity $\overline{M_{0,3,1}(\gamma)} = -3M_{2,1,1}(\gamma)$.

Yet another variation on the same theme is to consider the signed areas of triangles formed by a pair of random points on the curve and the center of mass of the region, which we have taken to be at the origin. The statistical distribution of these areas is again symmetric about zero, but its variance and kurtosis proved to be effective in discriminating shapes in the experiments. The second and fourth moments are given by

$$-\frac{|M_{2,0,0}(\gamma)|^2 - M_{1,1,0}(\gamma)^2}{2M_{0,0,0}(\gamma)^2} \quad \text{and} \quad \frac{|M_{4,0,0}(\gamma)|^2 - 4|M_{3,1,0}(\gamma)|^2 + 3M_{2,2,0}(\gamma)^2}{8M_{0,0,0}(\gamma)^2},$$

respectively.

While it is interesting that the moments of these shape distributions can be computed as contour integrals along the curve, they still belong to the classical picture, requiring only classical complex moments (be they of the region or of its boundary) for their effective computation. With varifold moments we can do more.

Distributions of signed distances from lines to points.

The n -th moment of the distribution of signed distances from tangent lines to the origin (center of mass) is given by the integral

$$\int_{\gamma} \Im \left(\frac{\bar{z}\dot{z}}{|\dot{z}|} \right)^n ds$$

divided by the perimeter of the curve. It turns out that the first moment equals twice the area of the region divided by its perimeter. Indeed,

$$\begin{aligned}
 \int_{\gamma} \Im \left(\frac{\bar{z}\dot{z}}{|\dot{z}|} \right) |\dot{z}| dt &= \frac{1}{2i} \int_{\gamma} (\bar{z}\dot{z} - z\bar{\dot{z}}) dt = \frac{1}{2i} \int_{\gamma} \bar{z} dz - \frac{1}{2i} \int_{\gamma} z d\bar{z} \\
 &= \frac{1}{i} \iint_D d\bar{z} \wedge dz,
 \end{aligned}$$

which is twice the area of the region enclosed by γ . The second moment of this distribution is given by the more interesting expression

$$\frac{M_{1,1,0}(\gamma) - \Re(M_{0,2,2}(\gamma))}{M_{0,0,0}(\gamma)}.$$

The n -th moment of the distribution of signed distances from normal lines to the origin (centre of mass) is given by the integral

$$\int_{\gamma} \Re \left(\frac{\bar{z}\dot{z}}{|\dot{z}|} \right)^n ds$$

divided by the perimeter of the curve. In this case, the first moment (the mean) is equal to zero. The second, third, and fourth moments are given by rather simple formulas:

$$m_2 = \frac{\Re(M_{0,2,2}(\gamma)) + M_{1,1,0}(\gamma)}{2M_{0,0,0}(\gamma)}, \quad m_3 = \frac{\Re(M_{0,3,3}(\gamma))}{4M_{0,0,0}(\gamma)},$$

$$m_4 = \frac{\Re(M_{0,4,4}(\gamma)) + 4\Re(M_{1,3,2}(\gamma)) + 3M_{2,2,0}(\gamma)}{8M_{0,0,0}(\gamma)}.$$

One last statistical distribution we wish to present is the distribution of oriented distances between a random tangent line and a random point on the curve. The n -th moment of this distribution is given by the integral

$$\iint_{\gamma \times \gamma} \Im \left((\bar{z}(s_1) - \bar{z}(s_2)) \frac{\dot{z}(s_1)}{|\dot{z}(s_1)|} \right)^n ds_1 ds_2$$

divided by the square of the perimeter. The mean or first moment of this distribution is again twice the area of the region divided by its perimeter, but the second moment is more interesting:

$$m_2 = \frac{\Re(-M_{0,2,0}(\gamma)M_{0,0,2}(\gamma) + 2M_{0,1,2}(\gamma)M_{0,1,0}(\gamma)) - M_{0,0,0}(\gamma)\Re(M_{0,2,2}(\gamma))}{2M_{0,0,0}(\gamma)^2}$$

$$+ \frac{M_{0,0,0}(\gamma)M_{1,1,0}(\gamma) - |M_{1,0,0}(\gamma)|^2}{M_{0,0,0}(\gamma)^2}.$$

APPENDIX C. IMPLEMENTATION DETAILS

C.1. Computer resources. This work was implemented in Python 3.10.12 and is publicly available at [<link to the code>](#). Unless otherwise specified, all experiments were conducted on a machine equipped with a 12th Gen Intel Core i5-12500 CPU and no GPU. Experiments involving ShapeEmbed [40], a variational autoencoder-based method, were performed on our institutional computing cluster, using an NVIDIA A40 GPU with 46 GB of GDDR6 memory (CUDA 13.2) and an AMD EPYC 7413 24-Core processor.

C.2. Details on the classifiers. The first classifier used is a Random Forest (**RF**) [93] with 800 trees, grown without depth restriction. At each node, the number of features considered for splitting is set to \sqrt{p} , where p is the total number of features. The minimum number of samples required to split an internal node and to form a leaf are both set to their default values of 2 and 1 respectively. Bootstrap sampling is enabled, meaning that each tree is trained on a random subset of the training data drawn with replacement. Since the same features, when computed with area normalization, can be highly correlated with the original ones, we remove those whose pairwise correlation exceeds a fixed threshold. Finally, we apply Recursive Feature Elimination [106] to select the most informative invariants for the classification task. The second classifier is a Multi-Layer Perceptron (MLP) implemented in PyTorch [107]. The network consists of two hidden layers followed by an output layer. The first hidden layer maps the input of dimension (number of invariants considered) to 256 neurons, and the second hidden layer reduces the representation to 128 neurons and the third one to 64, before the final output layer produces a score for each of the number of classes to classify. Each hidden layer follows the same structure: a fully connected linear transformation, Batch Normalization [108] to stabilize and accelerate training, a ReLU activation function [109] to introduce non-linearity, and a Dropout layer [110] with rate $p = 0.4$ to reduce overfitting. The output layer is a plain linear projection with no activation, as the loss function is expected to handle the final normalization. The network is trained by minimizing the Cross-Entropy loss for several hundred epochs, with early stopping based on validation accuracy and a fixed patience parameter, the best-performing model is retained. Given the relatively small size of the network, it can typically be trained for several epochs without requiring a GPU.

APPENDIX D. ADDITIONAL DETAIL ON DATASETS

D.1. Datasets of Geometric Shapes and Objects.

Mendeley. The Mendeley 2D shape benchmark [99] contains 9 classes of geometric objects (Triangle, Square, Pentagon, Hexagon, Heptagon, Octagon, Nangon, Circle and Star), each class instantiated with 10,000 samples. We examined a subset of the original dataset consisting of 1,000 randomly selected shapes per class (the selected seed will be available with the rest of the code) that exhibited significant variations in scaling, rotation, and deformation. This subset offers sufficient variability in terms of transformations while reducing the computational effort required for the experiments.

MNIST. The MNIST dataset ([96]) released under the GNU GPL, contains 70,000 handwritten digit from 0 to 9 in grayscale images with roughly 7,000 samples for each class.

MPEG-7. The MPEG-7 CE-Shape-1 Part B dataset [97], distributed under the LGPL-3.0 license, contains 1,400 binary masks of objects (animals, tools, and symbolic shapes, ect...) organized into 70 classes, with 20 samples in each class.

MPEG-400. The MPEG-400 dataset [98] contains 400 binary silhouettes (animals, tools, household items) grouped into 20 classes, each containing 20 samples. Notable variations in articulation, deformation, and viewing angle, make this dataset challenging for contour-based algorithms.

D.2. Datasets of Leaves:

Swedish Leaves. The Swedish leaves dataset [101] from the Linköping University, freely downloadable at <https://www.cvl.isy.liu.se/en/research/datasets/swedish-leaf/> under license CC BY 4.0, consists in pictures of leaves organized into 15 classes, with 75 leaves per class. This dataset is particularly challenging since leaves with peduncle and leaves without peduncle are present in the same class [87].

Flavia. . The Flavia dataset [100] contains 1,907 leaf images belonging to 32 classes, released under the GNU GPL and is available at <https://flavia.sourceforge.net/>. Achieving high classification accuracy on this dataset is challenging due to the larger number of classes and the extremely similar shapes among many of them. This dataset is particularly interesting after the samples have been randomly rotated, as it exhibits an orientation bias; that is, samples from the same class tend to be oriented in the same direction [87].

D.3. Datasets of Cells.

BBBC010. . The Broad Bioimage Benchmark Collection 10 [102] (BBBC010, no license) is a biological imaging dataset. It contains 1,407 individual binary masks of *C. elegans* nematodes divided into two classes, with 768 individuals labeled “alive” and 639 individuals labeled “dead”.

HeLa Kyoto. The HeLa Kyoto dataset [103] (CellCognition project, CC-BY 4.0 License) consists of fluorescence microscopy images of H2B-mCherry-stained HeLa Kyoto cell nuclei.

Already segmented and cropped masks for individual nuclei are available under the classifier data section of the dataset. We consider 313 objects in 4 classes that are representative of nuclei at key phases of mitosis: early anaphase (earlyana, 40 samples), lateana (lateana, 83 samples), metaphase (meta, 110 samples), and prometaphase (prometa, 80 samples).

Mouse Osteosarcoma Cells (MOC). The MOC dataset (MIT license, [104]) consists of fluorescence microscopy images of mouse osteosarcoma cells. In this dataset, cells have been exposed to cytoskeletal perturbation through treatment with the single drugs jasplakinolide (Jasp) and cytochalasin D (Cytd). The 649 cells are divided in 3 classes: a control class with 318 untreated cells, a Cytd class with 175 cells,

and a Jasp class with 156 cells.

D.4. Sample images. We provide some images of the different shapes considered inside each dataset in Fig. 2, Fig. 4, Fig. 5, Fig. 3, Fig. 6, Fig. 7, Fig 8, Fig 9, Fig. 10. These were extracted with different pipelines. Some dataset provided already the contour shapes (MOC [104]), other the 2D masks (MPEG-7 [97], MPEG-400 [98], BBBC010 [102] and HeLa Kyoto[103]) and from them we utilized the ShapeEmbed [40] pipeline to extract the boundaries, in order to have the most fair comparison. For the leaves datasets, we extracted directly the 2D contours from the images, relying on our pipeline, that will be shared with the rest of the code. In particular, for the BBBC010 dataset, by exploiting a confident learning approach, we identified that approximately 7% of the samples are incorrectly or misleadingly labeled. Examples of these mislabeled instances are shown in Fig. 11. We therefore introduce a cleaned version of the dataset, denoted cBBBC010, which is used to evaluate the different approaches; the results are reported in Table 5.

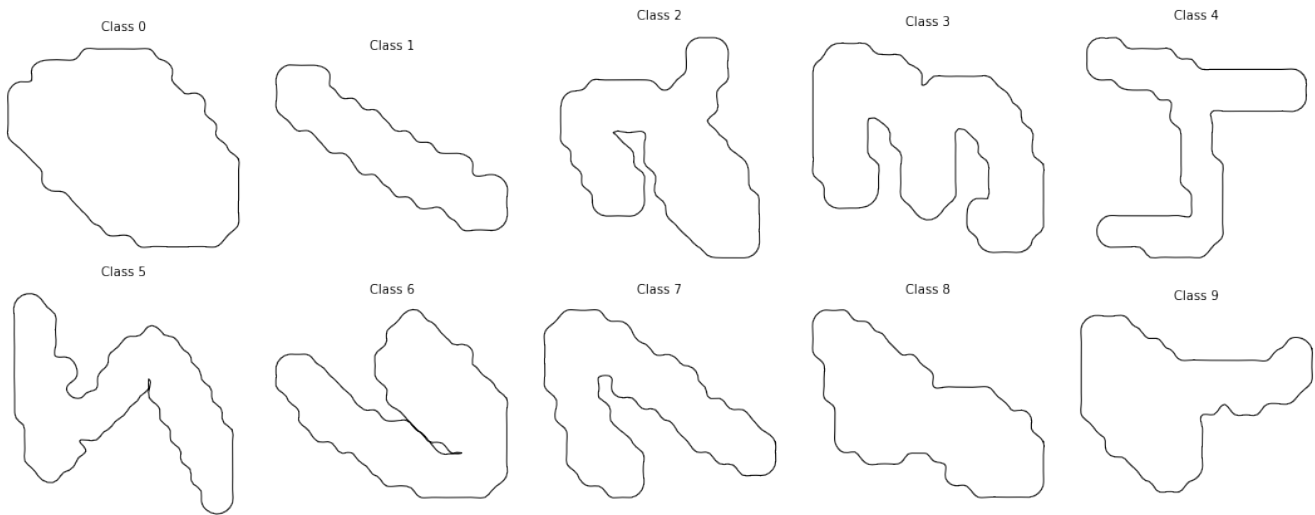


FIGURE 2. Visualization of random selected MNIST [96] shapes, one per class.

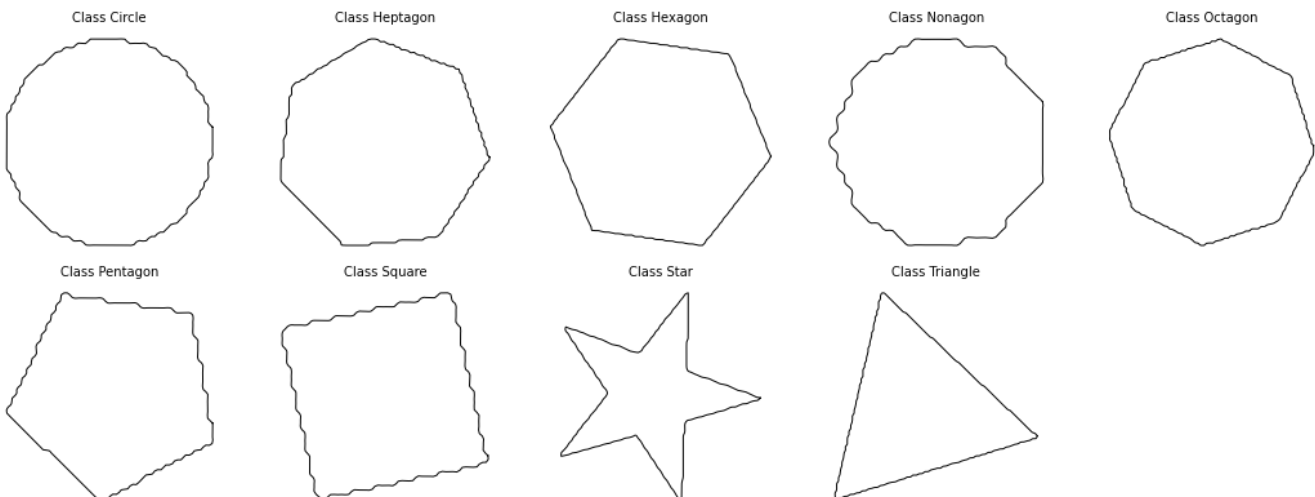


FIGURE 3. Visualization of random selected Mendeley [99] shapes, one per class.

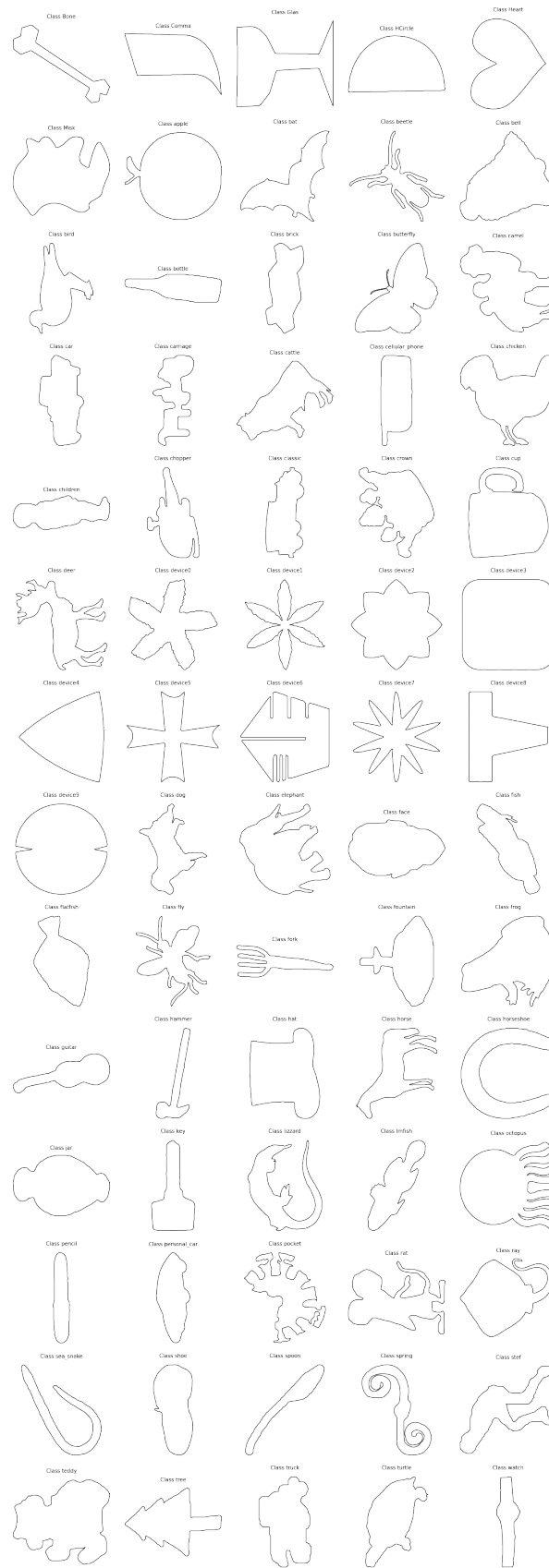


FIGURE 4. Visualization of random selected MPEG7 [97] shapes, one per class.

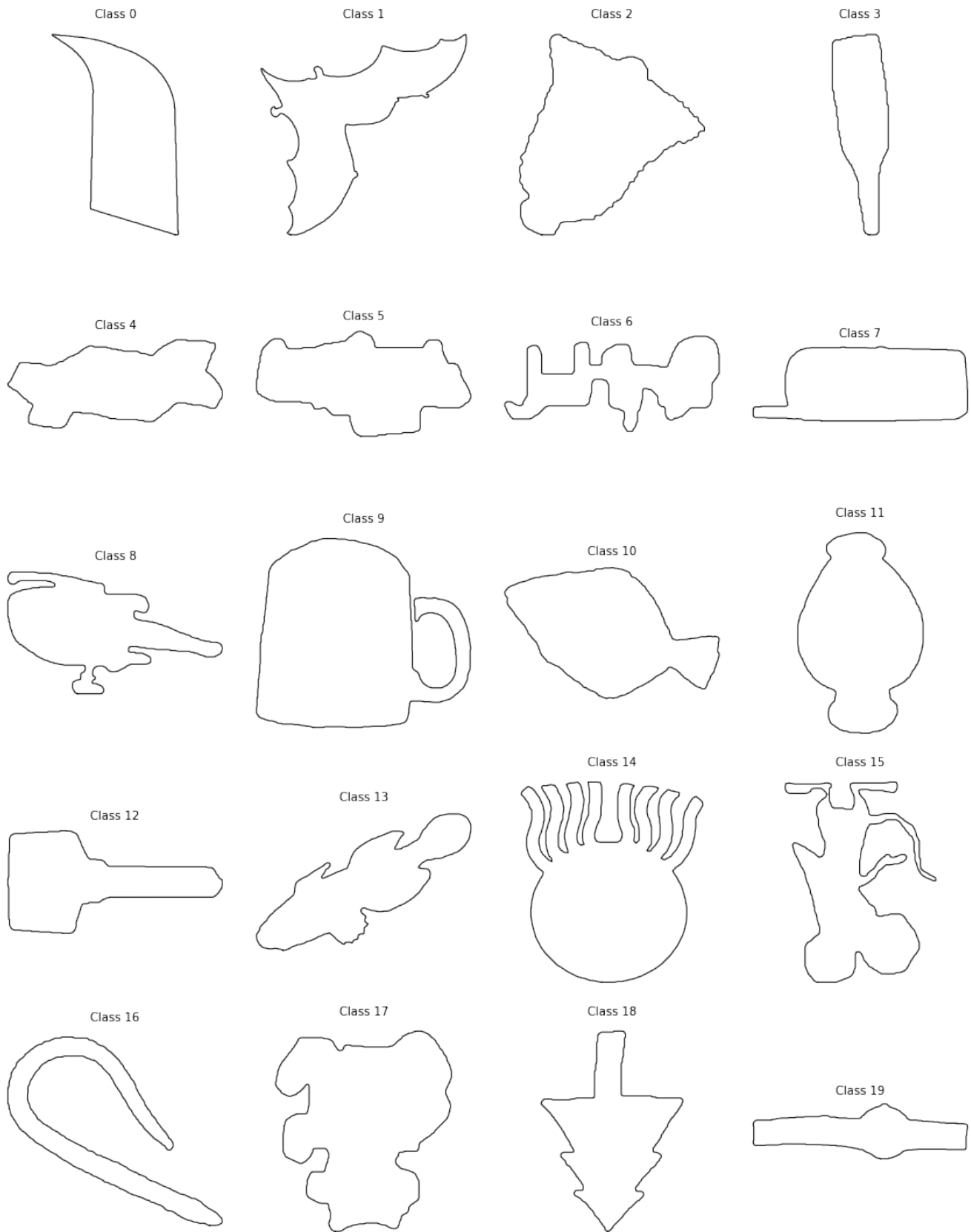


FIGURE 5. Visualization of random selected MPEG400 [98] shapes, one per class.

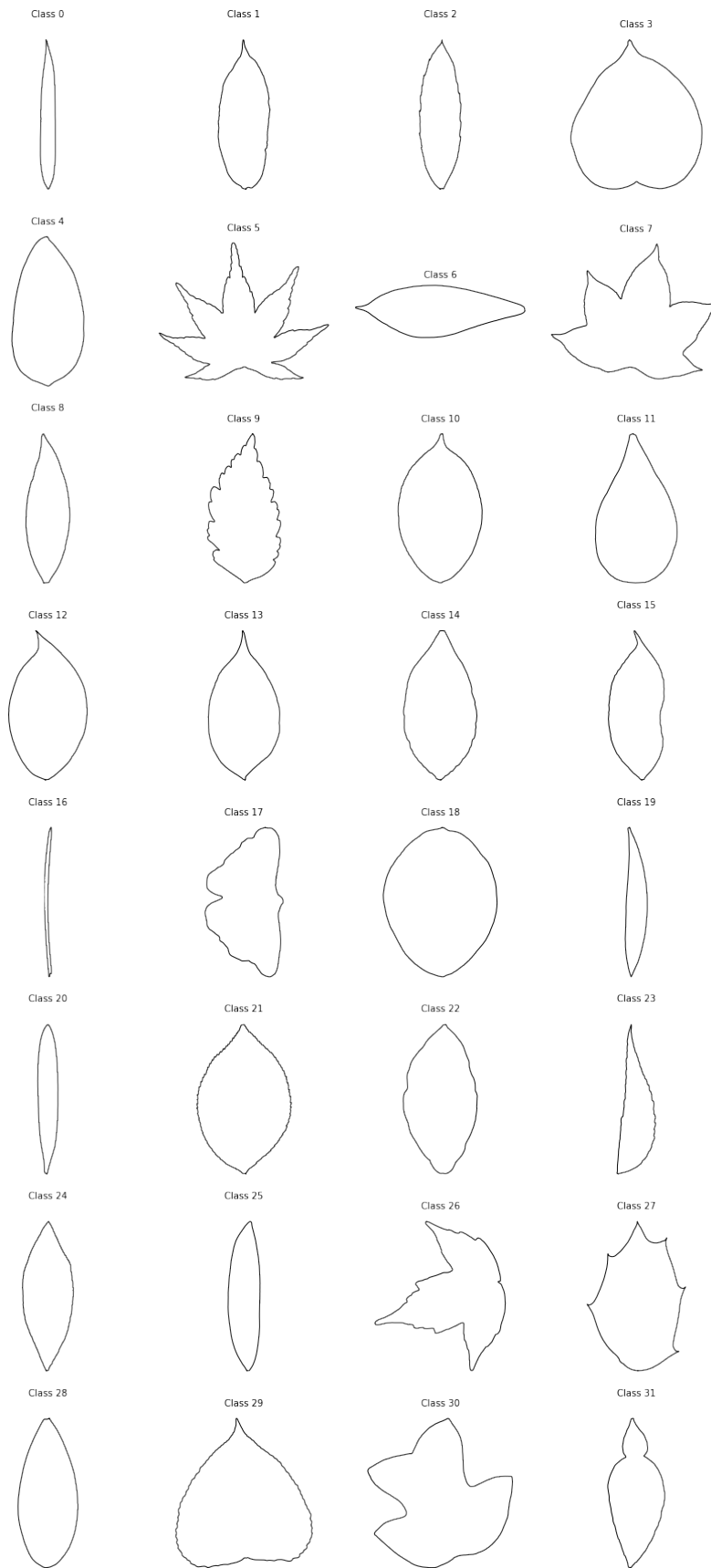


FIGURE 6. Visualization of random selected Flavia [100] shapes, one per class.

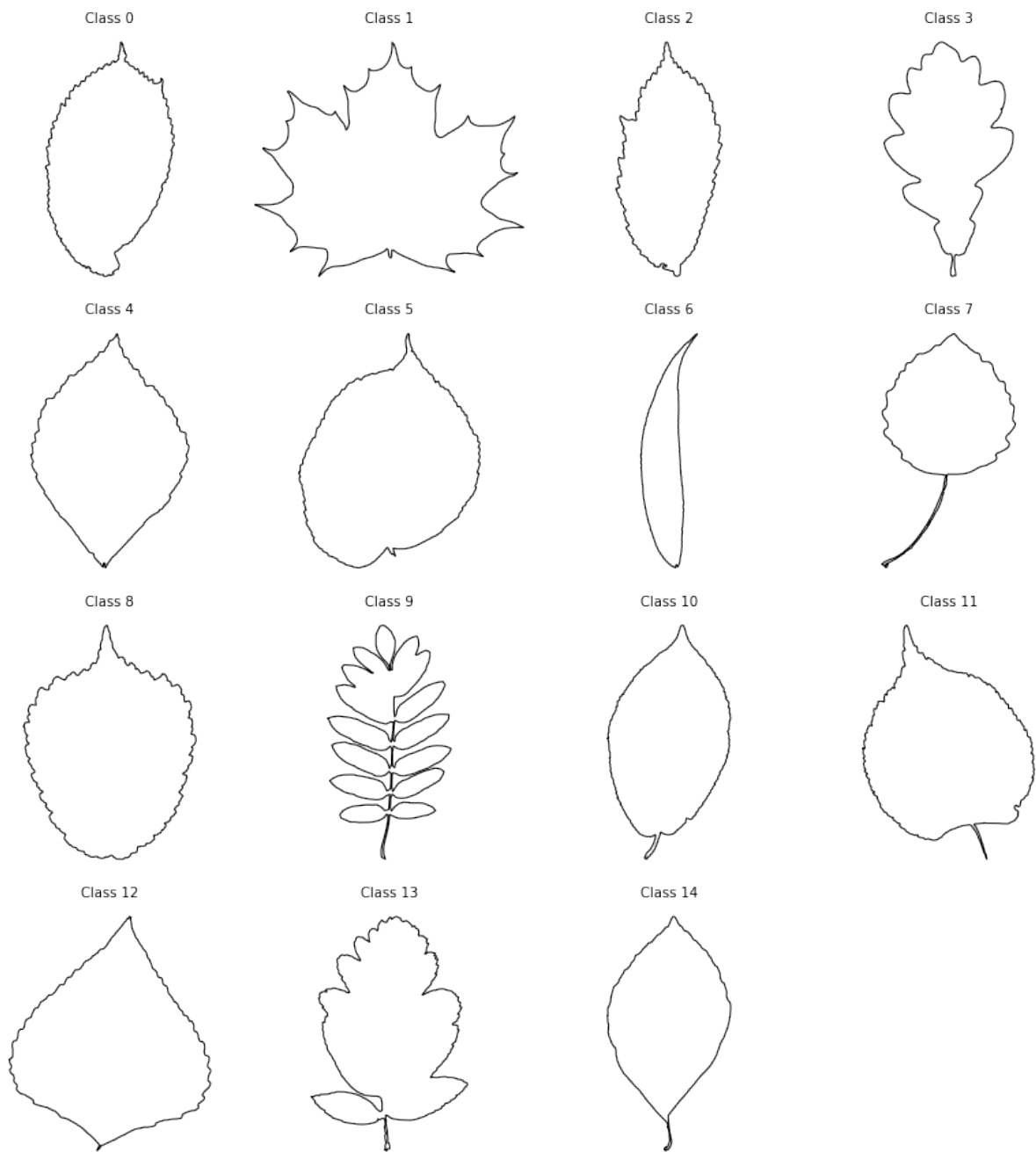


FIGURE 7. Visualization of random selected Swedish Leaves [101] shapes, one per class.



FIGURE 8. Visualization of random selected BBBC010 [102] shapes, one per class.

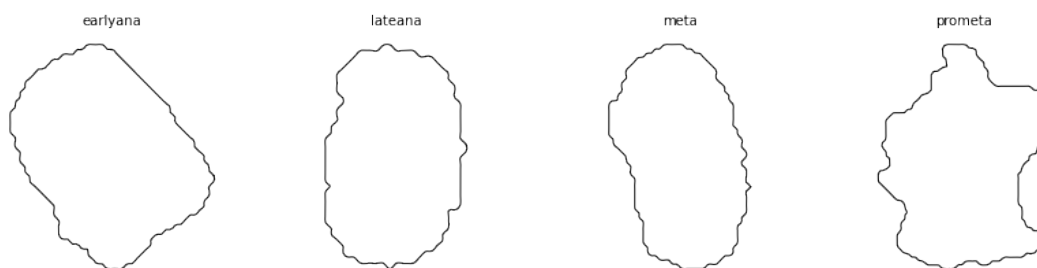


FIGURE 9. Visualization of random selected HeLa Kyoto [103] shapes, one per class.

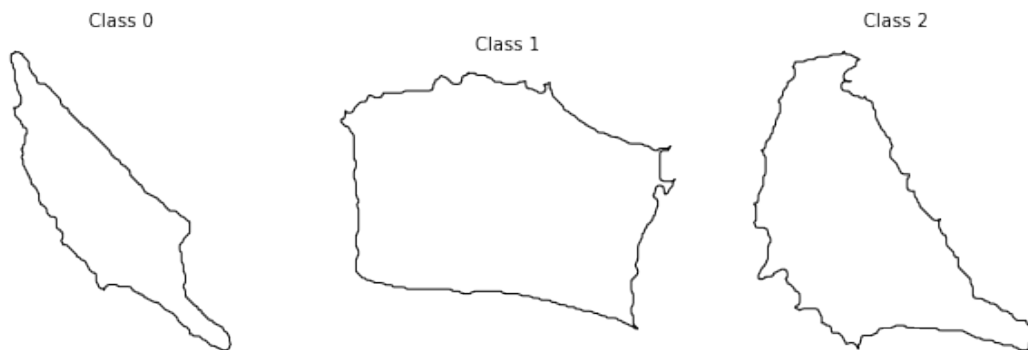


FIGURE 10. Visualization of random selected MOC [104] shapes, one per class.

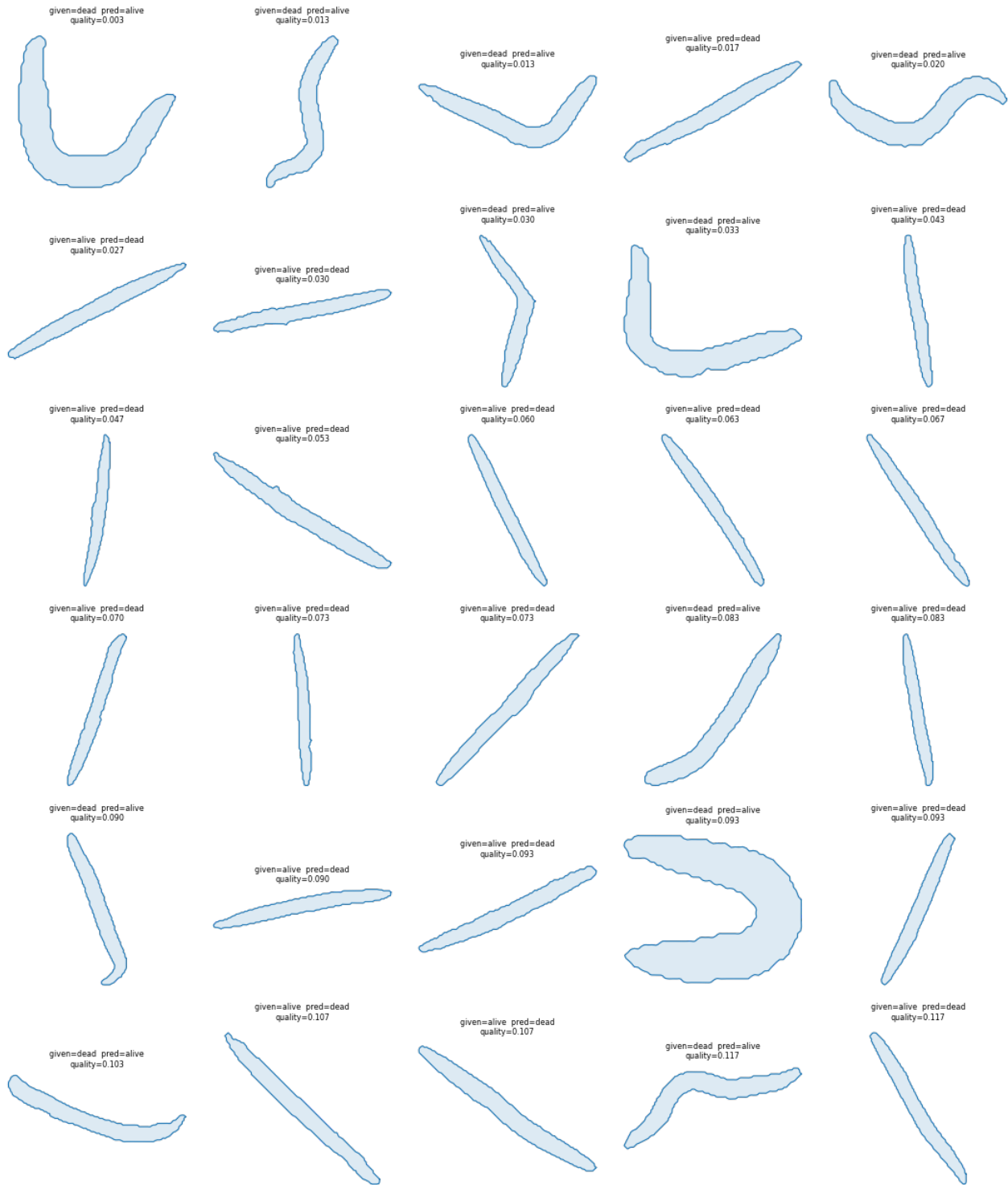


FIGURE 11. BBBC010 [102] samples identified as potentially mislabeled using a confident learning approach. For each sample, we report the assigned label (given), the model prediction (pred), and the associated confidence score (quality).

APPENDIX E. BASELINES IMPLEMENTATION DETAILS

Flusser. To provide a direct comparison with classical moment-based approaches, we implement the set of affine moment invariants introduced by Flusser [83]. These invariants are computed using the same complex-moment framework adopted for our Variance Moment Invariants (VMI), ensuring a consistent computational pipeline across methods. In our notation, the complex moment of order (p, q) is denoted by $\frac{1}{2i(q+1)}M_{p,q+1,1}$. The eleven Flusser invariants are then defined as follows:

$$\begin{aligned}
\bullet F_1 &= \frac{M_{1,2,1}}{4i} \\
\bullet F_2 &= \frac{M_{2,2,1}}{4i} \cdot \frac{M_{1,3,1}}{6i} \\
\bullet F_3 &= \Re \left(\frac{M_{2,1,1}}{2i} \cdot \left(\frac{M_{1,3,1}}{6i} \right)^2 \right) \\
\bullet F_4 &= \Im \left(\frac{M_{2,1,1}}{2i} \cdot \left(\frac{M_{1,3,1}}{6i} \right)^2 \right) \\
\bullet F_5 &= \Re \left(\frac{M_{3,1,1}}{2i} \cdot \left(\frac{M_{1,3,1}}{6i} \right)^3 \right) \\
\bullet F_6 &= \Im \left(\frac{M_{3,1,1}}{2i} \cdot \left(\frac{M_{1,3,1}}{6i} \right)^3 \right) \\
\bullet F_7 &= \frac{M_{2,3,1}}{6i} \\
\bullet F_8 &= \Re \left(\frac{M_{3,2,1}}{4i} \cdot \left(\frac{M_{1,3,1}}{6i} \right)^2 \right) \\
\bullet F_9 &= \Im \left(\frac{M_{3,2,1}}{4i} \cdot \left(\frac{M_{1,3,1}}{6i} \right)^2 \right) \\
\bullet F_{10} &= \Re \left(\frac{M_{4,1,1}}{2i} \cdot \left(\frac{M_{1,3,1}}{6i} \right)^4 \right) \\
\bullet F_{11} &= \Im \left(\frac{M_{4,1,1}}{2i} \cdot \left(\frac{M_{1,3,1}}{6i} \right)^4 \right)
\end{aligned}$$

EFD. The Elliptical Fourier Descriptors [19] were calculate utilizing the python library PYEFD (<https://pyefd.readthedocs.io/en/latest/>). Specifically, the contour coordinates are approximated by a truncated Fourier series, retaining the first K harmonics, where $K = 10$ in all experiments. Each harmonic contributes four coefficients, yielding a feature vector of dimension $4K=40$. To ensure invariance to translation, rotation, and scale, the descriptors are normalized following the standard EFD normalization procedure.

Region Properties. Region based shape descriptors are used as a classical baseline by extracting a set of geometric and moment based features from each segmented object. Given a closed contour, we first rasterize it into a binary mask. From each mask, we compute a collection of 19 standard morphological descriptors using the REGIONPROPS implementation from SCIKIT-IMAGE [26]. These features capture complementary aspects of object geometry, including size, elongation, convexity, and spatial extent. Specifically, the descriptor vector comprises: area, convex area, perimeter, major and minor axis lengths, extent, eccentricity, solidity, maximum Feret diameter, the seven invariant Hu moments, bounding-box height, bounding-box width, and bounding-box area. These quantities provide a compact summary of both global shape and spatial distribution.

XShapeEncoder. The method proposed by [36] introduces both equivariant and invariant approaches for contour embedding. In our experiments, we primarily employ the equivariant network implementation provided by the author at the following link <https://github.com/yuhanghe01/XShapeEnc> We further adapt the original code to extract invariant features, following the procedure described in the paper. Specifically, we retain only the magnitude of the Zernike basis projections. This modification reduces the feature dimensionality (absolute value instead of the real and imaginary components) and prevents the decoder from reconstructing the input shape in its original pose.

ShapeEmbed. To evaluate our main competitor, ShapeEmbed [40], we aligned our experimental protocol with that described in their work and we relied on the code available at <https://github.com/uhlmannngroup/ShapeEmbed>. Specifically, each contour was represented using 64 sampled points. For the MOC dataset, as done in the main paper, we utilized a 512 x 512 distance matrix, and the latent space dimension fixed to 128. For each dataset, we used an 80%/20% train-test split and evaluated classification performance using five-fold stratified cross-validation and tested them with the provided logistic regression

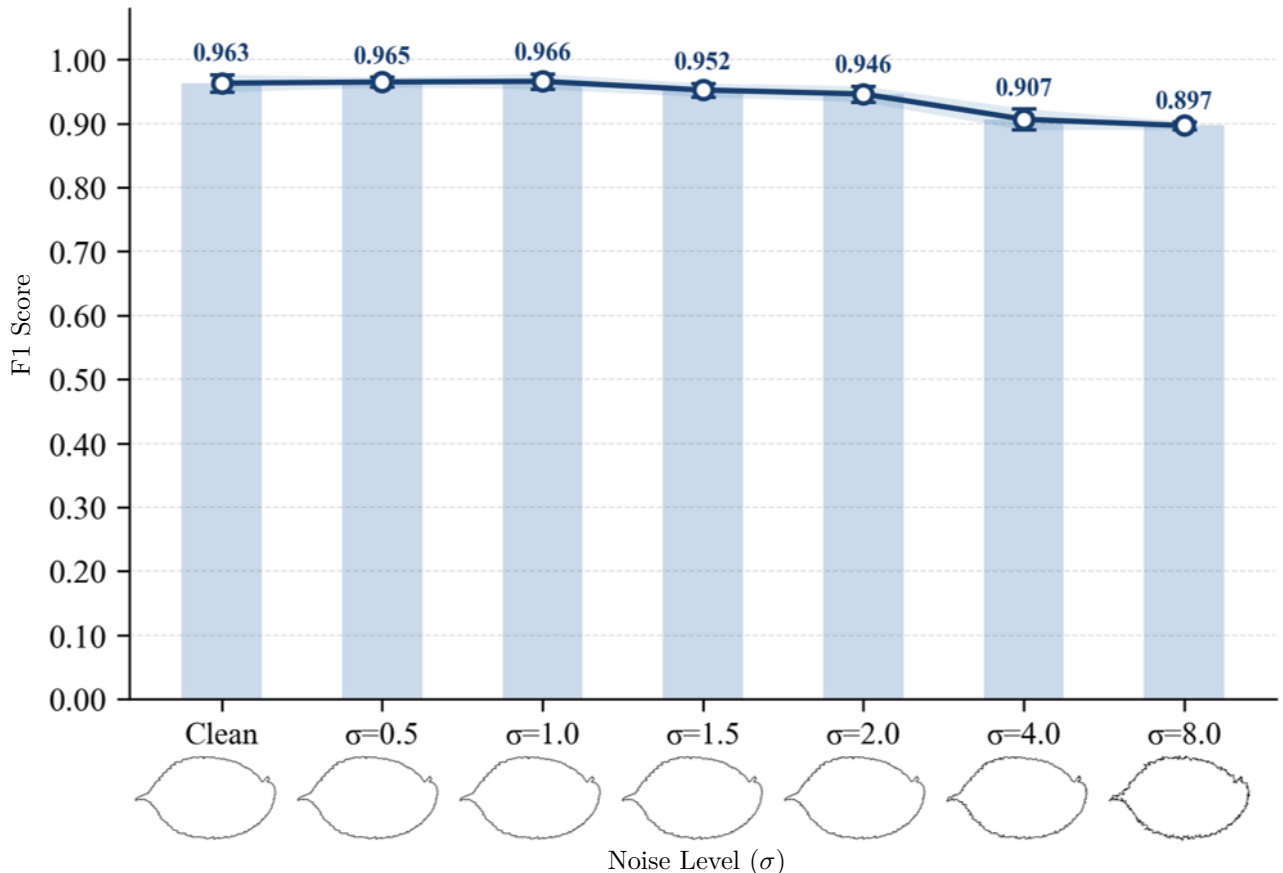


FIGURE 12. Robustness of VMI features in a classification task on the Swedish Leaves dataset [101] under Gaussian noise perturbations applied to the shape contours, evaluated in terms of F_1 -score (Higher the better).

[111].

APPENDIX F. ROBUSTNESS TO BOUNDARY PERTURBATIONS UNDER GAUSSIAN NOISE.

To evaluate the sensitivity of the proposed pipeline to shape corruption, we subject the complex contour representations to additive Gaussian noise of increasing magnitude. Formally, given a complex contour $\gamma \subset \mathbb{C}$, we construct perturbed variants $\tilde{\gamma} = \gamma + \varepsilon$, where $\varepsilon \sim \mathcal{CN}(0, \sigma^2)$ is drawn independently for each boundary point, with $\sigma \in \{0.5, 1.0, 1.5, 2.0, 4.0, 8.0\}$. As illustrated in Figure 12, low amplitude perturbations, up to ($\sigma = 1$), introduce subtle boundary irregularities while preserving global morphology, whereas higher noise levels ($\sigma > 2$) progressively erode class-discriminative geometric cues such as global structure, margin serrations, and overall silhouette. For each noise level, we extracted the features with VMI from the Swedish Leaves dataset and tested utilize the same Random Forest approach of all the other experiments. Performance is reported in terms of averaged Accuracy.

APPENDIX G. ROBUSTNESS UNDER SUCCESSIVE APPROXIMATIONS OF THE CONTOUR

To investigate the dependence of classification performance, and consequently feature quality, on the curve parameterization, we varied the number of vertices sampled along each contour and extracted features using the proposed pipeline. Table 6 reports the resulting classification performance for different number of equidistributed points along the contours. Additionally, it illustrates how the computational cost of the method scales with the number of sampled points. We observe that:

- Once the contour is sampled densely enough to approximate the underlying continuous curve, the Varifold Moment Invariants (VMI) exhibit strong robustness, yielding discriminative features for the classification task.
- The optimal number of sampled points is dataset-dependent. For instance, as shown in Table 6, datasets in which shape differences are primarily driven by size related features (e.g., the HeLa Kyoto dataset [103]) benefit from lower resolutions than those dominated by small geometric details. For datasets of leaves, (e.g. Flavia [100]), the boundary contain class-discriminating features that are capture with more accuracy with more points along the contours, leading to a slightly improvement of classification results with the increase of the resolution.
- The computational cost of VMI extraction scales linearly with the number of contour points, suggesting an overall complexity of $\mathcal{O}(N)$.

TABLE 6. Varifold Moment Invariants computed across different contour parameterizations. The table shows how varying the number of sampled points affects the F_1 score classification score (higher is better), as well as how the computational time increases approximately linearly.

Dataset	N_{points}	F_1 -Score	Time (s)
Flavia [100]	300	0.9551 ± 0.0085	347 sec
Flavia [100]	400	0.9578 ± 0.0081	467 sec
Flavia [100]	500	0.9595 ± 0.0103	573 sec
MPEG-7 [97]	300	0.9326 ± 0.0220	253 sec
MPEG-7 [97]	400	0.9265 ± 0.0187	327 sec
MPEG-7 [97]	500	0.9290 ± 0.0252	402 sec
HeLa Kyoto [103]	300	0.9359 ± 0.0379	57 sec
HeLa Kyoto [103]	400	0.9136 ± 0.0190	75 sec
HeLa Kyoto [103]	500	0.9278 ± 0.0350	91 sec

COMPUTER VISION LAB, TECHNISCHE UNIVERSITÄT WIEN, KARLSPLATZ 13, 1040 VIENNA, AUSTRIA, WOLFGANG PAULI INSTITUT, OSKAR-MORGENSTERNPLATZ 1, 1090 VIENNA, AUSTRIA

U.M.R. CNRS 8524, U.F.R. DE MATHÉMATIQUES, 59655 VILLENEUVE D’ASCQ CÉDEX, FRANCE

LABORATOIRE PAINLEVÉ, LILLE UNIVERSITY, 59650 VILLENEUVE D’ASCQ, FRANCE, WOLFGANG PAULI INSTITUT, OSKAR-MORGENSTERNPLATZ 1, 1090 VIENNA, AUSTRIA